Doctoral Dissertation

Three-dimensional simulation of droplet evaporation in attemperator

Yumi Uruno

Department of Mechanical Engineering

Graduate School

Korea University

February 2023

Three-dimensional simulation of droplet evaporation in attemperator

by
Yumi Uruno

---

under the supervision of Professor Jaewon Chung

A dissertation submitted in partial fulfillment of
the requirements for the degree of
Doctor of Philosophy.

Department of Mechanical Engineering

Graduate School

Korea University

October 2022

The dissertation of Yumi Uruno has been approved
by the dissertation committee in partial fulfillment of
the requirements for the degree of
Doctor of Philosophy.

December 2022

_____

Committee Chair: Jaewon Chung

_____

Committee Member: Yong Tae Kang

_____

Committee Member: Sam S. Yoon

_____

Committee Member: Seongkyun Im

_____

Committee Member: Hookyung Lee

Three-dimensional simulation of droplet evaporation in attemperator

by Yumi Uruno
Department of Mechanical Engineering
under the supervision of Professor Jaewon Chung

ABSTRACT

An attemperator (also called a desuperheater) sprays water into superheated steam to modulate its temperature to a desired set point. Here, the sprayed water must evaporate completely before it reaches the thermowell installed downstream of the attemperator, as the amount of water sprayed into the flow varies according to the steam temperature measured by the thermowell. Therefore, to develop optimal attemperator designs, it is vital to accurately predict the evaporation distance of the sprayed water and find suitable methods to reduce this distance.

In this study, measurements from the commissioning test of a coal-fired steam power plant were analyzed using transient analyses. These analyses compensated for the temperature change of spray water extracted far from the attemperator. By using these results for the enthalpy balance in the attemperator, the spray water flow could be calculated accurately enough to verify whether the spray-injected steam was completely desuperheated before the outlet thermowell or not, even during operations with changing the generator load.

In three-dimensional simulations, droplet breakup and evaporation in various attemperator design configurations were numerically simulated in the three-dimensional domain, considering both primary and secondary droplet breakup. The simulation model was validated by comparing the simulation results of four commissioning conditions (two for completely evaporated cases and two for not completely evaporated cases) with the corresponding transient thermal analysis results. Subsequently, four attemperator designs

were analyzed using the validated simulation model to obtain useful design insights. The simulation results demonstrated that all droplets should break up into droplets that are below a certain size to ensure complete evaporation. In addition, a venturi-type thermal liner can enhance droplet breakup by accelerating and decelerating the steam flow, resulting in faster droplet evaporation. Finally, the evaporation distance can be reduced by using multiple smaller-sized nozzles, which produce smaller initial droplets.

Keywords: attemperator, CFD, simulation, droplet evaporation, droplet breakup, superheated steam

과열저감기 내의 분사된 액적의 증발현상에 대한 3 차원 시뮬레이션 연구

우 루 노 유 미

기 계 공 학 과

지도교수: 정 재 원

국문 초록

과열저감기는 과열된 증기에 물 액적을 분사하여 원하는 설정점으로 온도를 조절한다. 분사된 액적은 과열저감기의 하류에 설치된 온도측정기에 도달하기 전에 완전히 증발해야 분사되는 물의 양을 적합하게 제어할 수 있다. 최적의 과열저감기 설계를 위하여 분사된 액적의 증발 거리를 예측하고 이 거리를 줄이는 방법을 찾는 것이 중요하다.

이 연구는 실제 과열저감기 구성에서 1 차 및 2 차 액적 분열을 모두 고려하여 3 차원 영역에서 수치적으로 시뮬레이션 하였다. 시뮬레이션 모델은 시운전데이터의 과도기상태에서의 열평형분석을 통하여 얻은 결과로부터 얻은 4 가지 시운전 조건과 비교하여 검증하였다. 검증된 시뮬레이션 모델을 사용하여 과열저감기의 설계 구성 변화에 따른 액적의 증발 경향을 관찰하기 위하여 4 개의 과열저감기 설계에 대하여 분석하였다.

시뮬레이션 결과로부터 분사된 물의 완전한 증발을 보장하기 위하여 모든 분사된 액적들이 특정 크기 미만의 액적으로 분열되어야 함을 보여주었다. 또한, 벤츄리 유형 보호관은 증기 속도를 가속 및 감속하여 액적 분열을 향상시켜 액적들의 증발을 더 빠르게 할 수 있었다. 마지막으로, 작은 초기 액적을 생성하는 작은 크기의 노즐을 여러 개 사용하면 증발 거리를 줄일 수 있음을 확인할 수 있었다.

중심어**:** 과열저감기, CFD, 시뮬레이션, 액적 증발, 액적 분열

Dedicated to my family

PREFACE

The research was supported by Basic Science Research Program through the National Research Foundation of Korea (NRF), which is funded by the Ministry of Education (NRF-2016R1D1A1B04933874) and by Doosan Heavy Industries and Construction Co. Ltd.

The contnets in Chapter 2 has been published in applied thermal engineering [Y. Uruno, G. Choi, M. Sung, J. Chung, H. Kim, K. Lee, Transient analysis of attemperator enthalpy balance based on the commissioning data of a coal-fired steam power plant, Appl. Therm. Eng. 150 (2019). https://doi.org/10.1016/j.applthermaleng.2019.01.047]. I was responsible of research method and data. Geuwon Choi was involved in the early stage of the project. Jaewon Chung was the supervisor of the project and manuscript edits.

The contents in Chapter 3 to 5 has been published in international journal of heat and mass transfer [Y. Uruno, J. Chung, H. Kim, K. Lee, Three-dimensional simulation of droplet breakup and evaporation in attemperator, Int. J. Heat Mass Transf. 196 (2022) 123300. https://doi.org/10.1016/j.ijheatmasstransfer.2022.123300] . I was the lead investigator and responsible for all data and manuscript. Jaewon Chung was the supervisor of the project and manuscript edits.

ACKNOWLEDGMENTS

Firstly, I would like to express my sincere gratitude to my advisor Prof. Jaewon Chung who made this work possible. He has taught me all knowledge related to research and helped me to overcome challenges during my Ph.D study.

I would like to thank the dissertation committee: Prof. Yong Tae Kang, Prof. Sam S. Yoon, Prof. Seongkyun Im and Dr. Hookyung Lee, for invaluable advice and feedback on my research. My dissertation could be improved with their helps.

I would like to thank to my lab members, Sangho, Hyunhun and Yoonseok who had helped me during the lab life. Also, the young members, Gyudong, Takhyun, Juwon, Sunghun, Geunyoung, of course Mogyu and Jihyun and Serang. Especially thanks for their friendship they show to me during my time in innovation hall and for always making me exciting.

On a personal level, I would like to thank the members of 515, Hyunjun, Heewon, Inseob, Hyein, Minhye, I could have encourage to finish my Ph.D because of you. My thanks also go out to the support I receive from Dokwan and Hyojun. As a senior in the Ph.D program, they gave me a lot of advice. Especially, Yoonseon, who always worried about my health. Also, thanks to my 2011 member of Mechanical Engineering.

TABLE OF CONTENTS

LIST OF TABLES

LIST OF FIGURES

NOMENCLATURE

A	area
Bi	Biot number
C_p	heat capacity of pipe
c_p	specific heat
C_{TW}	heat capacity of thermowell
d	diameter
d_{32}	Sauter mean diameter (SMD)
E	impact energy
F	force
h	specific enthalpy
h	heat transfer coefficient
h_{fg}	latent heat of vaporization
h_0	film height
k	thermal conductivity
L	pipe length
Nu	Nusselt number
m	mass
$\dot{m}$	mass flow rate
P	Pressure

P	perimeter
Pr	Prandtl number
Re	Reynolds number
S	source
T	temperature
t	time
T_{TW}	temperature measured by thermowell
T_P	temperature of pipe
u	velocity difference between steam and droplet
V_{ave}	average flow velocity
V	absolute velocity
V	volume
We	Weber number

Greek symbols

$crit$	critical
ρ	density
λ	radial integral length scale at the jet exit based on fully developed turbulent pipe flow
σ	surface tension of the liquid
δ_{bl}	boundary layer thickness,

μ	fluid viscosity
τ	thermal time constant

Subscripts

@	measured at
#1	1st attemperator
#2	2nd attemperator
$crit$	critical
cal	calculated
d	droplet
$delay$	time delay
$desuper$	de-superheated
$drag$	drag
eff	effective
$gravity$	gravity
i	inner
i	grid number
in	inlet
$meas$	measured
n	time step
n	normal
o	outer

out	outlet
P	pipe
sat	saturation
s	steam
w	wall
$water$	water

Power plant terminology

ATMP	attemperator
BCP	boiler circulation pump
BIF	bifurcation point of the water line into the 1st and 2nd attemperator
EC	economizer
FWH	feed water heater
HPT	high pressure turbine
SEP	separator
SH	superheater
STM	steam
TCV	throttle control valve
TW	thermowell

CHAPTER 1. INTRODUCTION

The increase in renewable energy production, such as from wind or solar power, has led to an increased demand for higher flexibility in conventional coal-fired power plants to maintain grid stability [1–5].

For example, the power generation of conventional power plant in Germany during ten days in November 2016 is shown in Figure 1. As can be seen in Figure 1, the generation of coal power plants decrease dramatically when the renewable power generation (solar, wind) is high (see 20th to 21st). On the other hand, when the renewable power generation is low (23rd to 24th), the coal power generation increases up to 40GW, which is half of the required power generation. The increasing renewable power generation is global phenomenon.

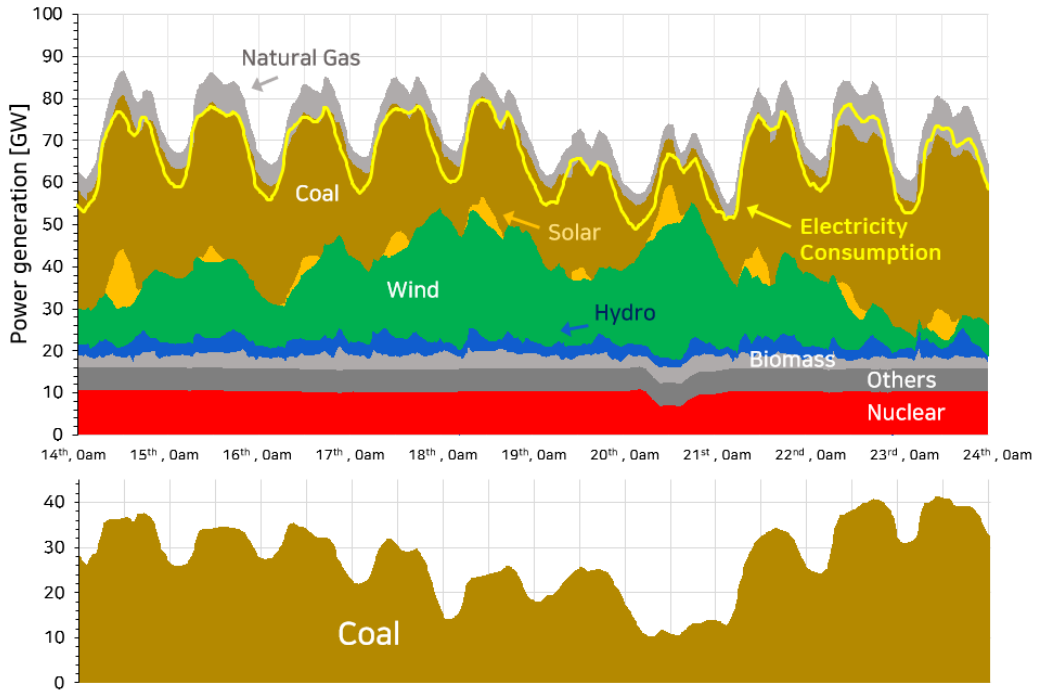

Figure 1 Conventional power plant in Germany during ten days in November 2016 [2]

Also, recently, Korea government published the 9th demand supply program on 2020.

Here, the power generation of renewable energies will be increase up to 40.9% until 2034 (it is 15.8% on 2020). Among the renewable energies, the solar and wind power plants possess the 91% [6]. As mentioned in Germany data, the power generation of solar, wind energies depend on weather, therefore, it is not predictable. Because of the non-uniform power generation, the possibility of large scale of black out is increases. Therefore, to prevent the problem, the coal power plants flexibility is required.

An attemperator (also called a desuperheater) can actively control the temperature of superheated steam and reduce it to a desired set point by injecting cold water into the superheated steam (Figure 2).

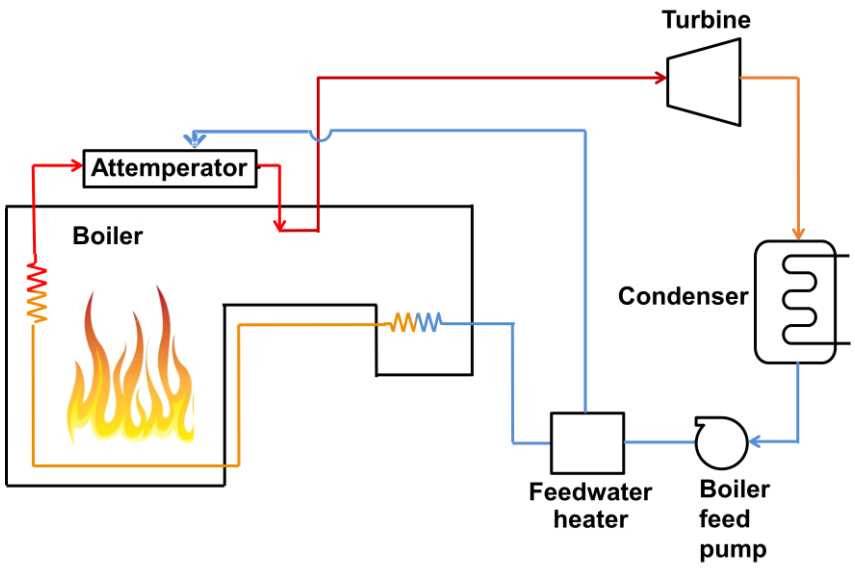

Figure 2 Simple schematic diagram of a coal-fired power plant

1.1 Attemperator

1.1.1 The role of attemperator

The amount of cold water injected by the attemperator is varied based on the steam temperature measured by a thermowell installed downstream of the attemperator. To ensure that the thermowell only records the desuperheated steam temperature and does not provide false feedback to the attemperator control system, the injected water must evaporate completely before it reaches the thermowell. Therefore, considering the design of an attemperator, the thermowell should be installed far downstream of the nozzle to ensure that there is enough distance for complete evaporation of the sprayed water. As shown in Figure 2, a thermal sleeve protects the main pipe from the thermal stress caused by the impact of the sprayed water droplets [7].

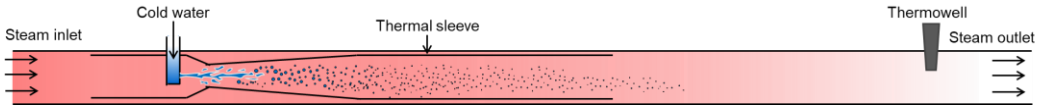

Figure 3 Schematic diagram of the attemperator

1.1.2 Components of attemperator

An attemperator is typically composed of a nozzle that injects a fine spray of water and a thermal sleeve to protect the main steam pipe against thermal shock due to the direct impingement of sprayed droplets (Figure 3). The desuperheated temperature is monitored through a thermowell installed at the outlet of the attemperator. This temperature sensor is tied to the feedback control of the spray water, which operates the control valve located between a feedwater heater and an attemperator

1.2 Previous work of attemperator

1.2.1 Numerical simulation of spray evaporation

The spray evaporation application is used in wide industries. The turbulence effect on mixing and evaporation of dilute spray is analyzed by Sadiki et al. and k-epsilon RANS model is used [8]. Guo et al. studied the spray evaporation in desulfurization wastewater by considering the initial droplet size distribution. The influence of velocity difference between the droplet and air on heat transfer is analyzed and conclusion is carried out that the high velocity difference increase the heat transfer however because of short residence time could lead to long evaporation distance [9]. Feng et al. also simulate the spraying system in flue gas desulfurization wastewater. They also considered how the velocity difference affect the spray evaporation. When considering the effect of velocity difference in droplet evaporation, the breakup would be most important factor, however, they did not consider the breakup effect. The simulation of spray cooling system in urban environment is carried out by Montazeri et al. [10]. The simulation considered the initial droplet size with Rossin-Rammler distribution, and the turbulence effect is calculated by RANS model. The results of spray evaporation were carried out varying the air speed and temperature. Samimi et al. developed the droplet collision model in multi-component fuel spray evaporation considering the turbulence [11]. However, these studies did not consider the real geometry of application which means that their simulations are conducted in simple geometry.

1.2.2 Numerical simulation of attemperator

As the spray cooling of superheated steam involves several complex physical processes, the analysis of an attemperator is a significant challenge. Schoonover et al. [12] performed a one-dimensional numerical simulation to predict the steam temperature change in an attemperator, considering the evaporation of the sprayed water droplets and assuming a monodisperse droplet size. Rahimi et al. [13] and Kouhikamali et al. [14] performed two-dimensional simulations by varying the initial droplet size and pipe diameter, and also assuming a monodisperse droplet size. These studies revealed that smaller initial droplets evaporate faster owing to their large surface-to-volume ratio. However, it should be noted

that the droplet breakup process was not considered in these studies.

In general, droplet breakup can be classified into two regimes: primary breakup and secondary breakup. Primary breakup occurs due to the disintegration of the liquid jet ejected from the nozzle, whereas secondary breakup occurs due to the drag force acting on the droplets owing to the velocity difference between the droplets and the steam.

Several scholars have considered the secondary breakup model proposed by Reitz [15] for attemperator systems. Cho et al. [16] performed a one-dimensional simulation to calculate the evaporation distance of droplets injected into superheated steam using the secondary breakup model. Ebrahiman and Gorgi–Bandpy [17] also employed the secondary breakup model to predict the droplet evaporation rate in an axisymmetric two-dimensional domain. These studies demonstrated that secondary breakup has a significant effect on the evaporation distance in an attemperator. However, both studies assumed monodisperse initial droplets (i.e. the size distribution of the droplets resulting from primary breakup was not considered).

Table 1 summarizes the physics considered in previous study of numerical simulation of attemperator system and this study.

Table 1 Summary of numerical simulation studies of attemperator system

Authors	Dimensions	Initial droplet size	Droplet breakup	Droplet collision	Turbulence	Geometry
Schoonover et al. [12]	1	monodisperse	-	-	-	-
Rahimi et al. [13]	2	monodisperse	-	-	-	Rectangle
Kouhikamali et al. [14]	2	monodisperse	-	-	-	Rectangle
Cho et al. [16]	1	monodisperse	Secondary breakup	-	-	-
Ebrahiman and Gorgi-Bandpy [17]	2	monodisperse	Secondary breakup	-	-	Rectangle
This study	3	Rossin-Rammler distribution	Secondary breakup	O'Rourke model	RANS (k-epsilon model)	Real geometry

1.3 Objective of this study

Since the experiments of attemperator is hard challenge due to the supercritical conditions (high temperatures and pressure and large mass flow rate), the studies of attemperator is highly depends on the simulation.

However, in-depth studies that consider the droplet size distribution resulting from primary and secondary breakup have not been conducted. Furthermore, the actual three-dimensional system has a complex stream velocity field that significantly affects the droplet breakup phenomena; however, previous studies generally fail to simulate these phenomena as one- or two-dimensional cases were considered.

Also, the validation of simulation is carried out by comparing the outlet temperature of experiments and simulations. However, this is meaningful only when the measured temperature is accurate. If the sprayed water from attemperator is not completely evaporated, the thermowell would measure wrong steam temperature, resulting in not accurate validation of simulations.

In this study, the commissioning data which will compare to the results of three-dimensional simulation is analyzed using enthalpy balance. The complete evaporation of sprayed water will confirm and the results will be used for the validation factor of simulation.

In three-dimensional simulation, the droplet breakup and evaporation phenomena in an actual attemperator geometry with reasonable accuracy is considered to provide design guidance for attemperator systems. Accordingly, three-dimensional numerical simulations are performed using ANSYS Fluent 19.1, considering both primary and secondary droplet breakup. For validation, the simulations were performed under four commissioning conditions of the attemperator and compared with the results from a previous study. Subsequently, the four design modifications were simulated.

The rest of this paper is organized as follows. Chapter 2 describes the transient analysis of commissioning data of coal-fired power plant. Chapter 3 describes the assumptions and models used in the numerical simulation considering the operating conditions of the attemperator; the results of the grid and convergence tests are presented as well. Chapter 4

presents the simulation results under four commissioning conditions and the accuracy of the simulation is validated by comparing the simulation results with the corresponding transient thermal analysis results from a previous study. Chapter 5 presents the simulation results of various attemperator designs that can provide useful design insights, and Chapter 6 discusses the results obtained in this study. Finally, Chapter 7 summarizes the study.

CHAPTER 2. TRANSIENT ANALYSIS OF COMMISSIONING DATA (THE VALIDATION DATA FOR THRE E-DIMENSIONAL SIMULATION)

The measurements from the commissioning test of a coal-fired steam power plant were analyzed using transient analyses. These analyses compensated for delayed temperature measurement at thermowells with large heat capacities and the temperature change of spray water extracted far from the attemperator. By using these results for the enthalpy balance in the attemperator, the spray water flow could be calculated accurately enough to verify whether the spray-injected steam was completely desuperheated before the outlet thermowell or not, even during operations with changing the generator load. Temperature readings from thermowells depend on the subcritical and supercritical conditions and the validity of the various simplifications used in the transient analysis were discussed. According to the transient analysis of the commissioning data, the thermowell distance in one of the attemperators could be judged as being too short to ensure complete desuperheating of the spray-injected steam, and thus, this should be considered in the control logic.

The temperature delayed due to the thermowell heat capacity is called thermowell transient (TT) analysis [7]. In this section, the temperature change of spray water extracted far from the attemperator is calculated. The accuracy of transient analysis using the calibrated temperature of sprayed water is increased compared to the TT analysis.

2.1 Enthalpy balance for the attemperator during a constant load operation

The attemperator (ATMP) injects spray water to desuperheat superheated steam (Figure 3). Thus, the enthalpy of the inlet superheated steam plus the spray water should equal that of the outlet desuperheated steam as shown in the following enthalpy balance equation:

$$\dot{m}_{s,in}h_{s,in} + \dot{m}_w h_w = \left(\dot{m}_{s,in} + \dot{m}_w\right)h_{s,out} \quad (1)$$

Here, $\dot{m}_{s,in}$ and $\dot{m}_w$ represent the steam and spray water mass flows, respectively. $h_{s,in}$, $h_{s,out}$ and h_w are respectively the specific enthalpy of the inlet steam, outlet steam and the spray water injected into the attemperator.

If the spray water completely evaporates ahead of the outlet thermowell and the steam temperatures at the inlet and the outlet of the attemperators remain constant, the respective thermowell measurements ($T_{TW,s@ATMP_{in}}$ and $T_{TW,s@ATMP_{out}}$) will reflect the temperatures of the incoming steam and the completely desuperheated steam ($T_{s,in}$ and $T_{s,out}$), respectively. Thus, thermowell temperature measurements can be directly used to obtain the respective enthalpies in Eq. (1). Using these values, the spray water flow ($\dot{m}_{w,cal}$) can be calculated using Eq. (2), and will agree well with the measured flow ($\dot{m}_{w,meas}$).

$$\dot{m}_{w,cal} = \dot{m}_{s,in}\frac{h_{s,in} - h_{s,out}}{h_{s,out} - h_w} \quad (2)$$

On the other hand, if the sprayed water did not completely evaporate ahead of the outlet thermowell, the thermowell would measure a temperature different from that of the completely desuperheated steam (i.e., $T_{TW,s@ATMP_{out}} \neq T_{s,out}$). In this case, the calculated spray water flow ($\dot{m}_{w,cal}$) using the enthalpy obtained $T_{TW,s@ATMP_{out}}$ will be different from the true measured one ($\dot{m}_{w,meas}$).

Therefore, by comparing $\dot{m}_{w,meas}$ and $\dot{m}_{w,cal}$ by Eq. (2) (i.e., by checking the enthalpy balance), it is possible to verify whether the spray injected steam was completely desuperheated ahead of the outlet thermowell or not.

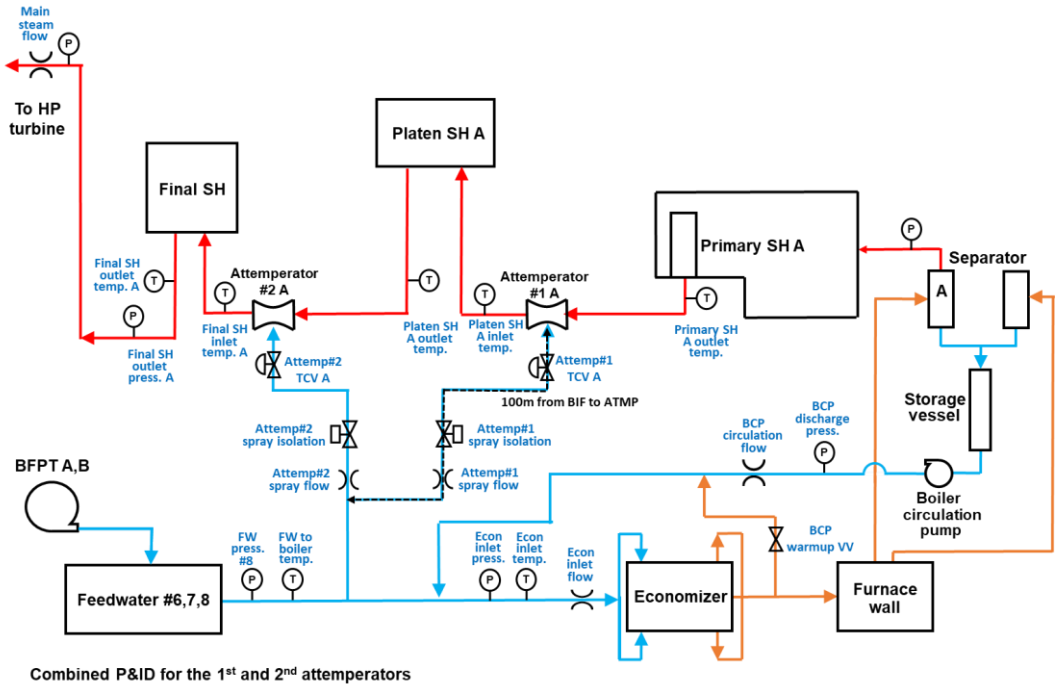

Figure 4 Combined piping and instrumentation diagram (P&ID) for the 1st and 2nd attemperators.

2.2 Estimation of the temperature of the spray water injected into the attemperator considering the heat transfer between fluid and pipe (fluid and pipe transient (FPT) analysis)

Under constant load operation, the water temperature at the feedwater heater outlet (Figure 4) is kept almost constant. Thus, both the internal fluid and the pipe wall is well insulated. That is, the temperatures will not change as the fluid flows through the pipe. In this case, the temperature of the spray water injected the attemperators would be the same as the temperature measured at the feedwater heater outlet (*TTW,w@FWH*).

On the other hand, during changing load operations (e.g. start-up, shut-down, loading change), the fluid temperature changes continuously, and the pipe wall responds slowly to changes in fluid temperature due to its relatively large thermal mass. Thus, when *TTW,w@FWH* begins to increase, the response of the temperature of the spray water injected into the attemperators will be delayed by the transport time of fluid in the pipe from the feedwater heater to the attemperator. In addition, since the fluid will lose heat as it flows through the cold pipe, the spray temperature will be smaller than *TTW,w@FWH* even after this transport time [18–20]. The starting point in this analysis is the unsteady energy equation for the fluid, assuming that the axial conduction is negligible (Figure 5).

$$\rho c_p A_i \left(\frac{\partial T}{\partial t} + V_{ave}\frac{\partial T}{\partial x}\right) = hP(T_p - T) \tag{3}$$

Here, ρ, c_p, A_i and P represent the density and specific heat of the fluid and the inner area and perimeter of pipe, respectively. T, T_p and V_{ave} respectively represent the fluid and pipe temperatures and the average flow velocity. Thus, the term on the right side of Eq. (3) represents the heat transfer between the inner flow and the pipe wall.

Here, quasi-steady heat transfer was assumed [21]; thus steady-state heat transfer coefficients could be obtained from the Dittus-Boelter equation.

$$Nu_{D_i} = 0.023 Re_{D_i}^{4/5} Pr^n \quad \text{if } 0.7 \le Pr \le 160 \text{ and } Re_{D_i} \ge 10{,}000 \tag{4}$$

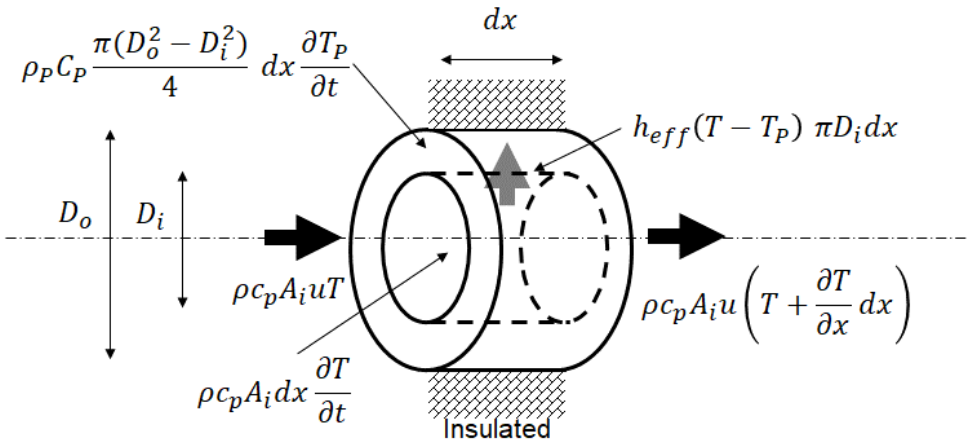

Figure 5 Energy balance for the control volume of fluid and pipe

Here, n = 0.4 for heating and n = 0.3 for cooling. Using the above correlation, the heat transfer coefficient ($h = Nu\ k/Di$) could be obtained. If the temperature gradient across the thickness of the pipe wall was small, the rate of heat loss at the surface of the pipe wall should be balanced by the rate of change of the internal energy of the pipe wall [22].

$$h_{eff} P(T - T_P) = \rho_P C_P (A_o - A_i) \frac{\partial T_P}{\partial t} \quad (5)$$

Here, P and CP represent the density and specific heat of the pipe, respectively. Combining Eqs. (1) and (3), the following governing equation can be obtained.

$$\frac{\rho c_p D_i}{4}\left(\frac{\partial T}{\partial t} + u\frac{\partial T}{\partial x}\right) = h(T_P - T) = -\rho_P C_P \frac{(D_o^2 - D_i^2)}{4D_i}\frac{\partial T_P}{\partial t} \quad (6)$$

The Biot number is larger than 10 under the current conditions; thus the effective heat transfer coefficient (*heff*) is again employed [25,26]. For fluid flow inside a solid pipe, the effective heat transfer coefficient can be obtained as follows:

$$h_{eff} = \left(\frac{1}{h} + \frac{1}{k_P}\frac{D_i^3(4D_o^2 - D_i^2) + D_i D_o^4 (4Ln[D_o/D_i] - 3)}{8(D_o^2 - D_i^2)^2}\right)^{-1} \quad (7)$$

Here, the time constant for the pipe wall, p can be expressed as Eq. (6).

$$\tau_p = \frac{\rho_P C_P \left(D_o{}^2 - D_i{}^2\right)}{4hD_i} \tag{8}$$

In this work, the fluid temperature at x = 0 (i.e., i = 0) for every time step can be obtained from the temperature measured at the thermowell (e.g. *TTW,w@FWH*) and the temperatures of the fluid and the pipe wall at the previous time step are known. Thus, Eq. (4) was explicitly discretized using an upwind method with forward differencing in time.

$$T_i^{n+1} = T_i^n + \left(-u_i^n \frac{T_i^n - T_{i-1}^n}{\Delta x} + \frac{4h_{eff}}{\rho c_p D_i}\left(T_{p_i}{}^n - T_i^n\right)\right)\Delta t \tag{9}$$

with $T_0^n = T_{TW,w@FWH}(t = n\Delta t)$

Here, $u\Delta t/\Delta x$ should be smaller than 1 to satisfy the stability requirement. Using the fluid temperature obtained at the new time step, the pipe temperature is obtained as follows:

$$T_{P_i}{}^{n+1} = T_{P_i}{}^n + \left(\frac{4h_{eff}D_i}{\rho_P C_P \left(D_o{}^2 - D_i{}^2\right)}\left(T_i^{n+1} - T_{P_i}{}^n\right)\right)\Delta t \tag{10}$$

Hereafter, these (Eqs. (7) and (8)) are referred to as the "Fluid and Pipe Transient (FPT)" analysis. In Figure 6, the fluid temperature measured at the economizer inlet (*TTW,w@EC*)was compared to that calculated (*Tw,EC,cal*) using Eqs. (7) and (8). Here, *Tw,EC,cal* was obtained from the temperatures measured at the feedwater heater outlet (*TTW,w@FWH* where x = 0 m) 120m ahead of the economizer. In addition, the thermophysical properties and geometric dimensions of pipe between the feedwater heater (FWH, x = 0 m) and the economizer (EC, x = 120 m) are summarized in Table 1. Here, the thermal time constant for the pipe wall (*p*) was calculated to be approximately 7 min, thus the pipe temperature (*TP,FWH,cal* and *TP,EC,cal*) responded slowly to increasing fluid temperature.

On the other hand, the time delay of the flow (*tdelay*) is as short as 0.5 min, since the flow speed is relatively fast (3.5 m/s). Therefore, the water temperature does not change much when flowing from FWH to EC (i.e., *TTW,w@FWH TTW,w@EC*), and the pipe temperature from FHW to EC also does not change much (i.e., *TP,FWH,cal TP,EC,cal*). As

a result, the calculated fluid temperature at the economizer (*Tw,EC,cal*) was in good agreement with the measured one (*TTW,w@EC*), as shown in Figure 6. Thus, the validity of the fluid and pipe transient (FPT) analysis could be verified.

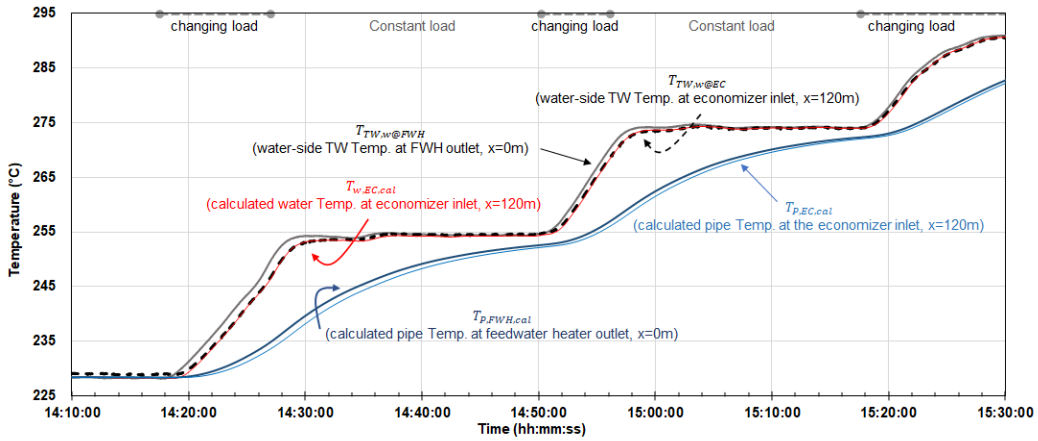

Figure 6 The results of a transient analysis to predict the fluid and pipe temperatures

Table 2 Thermophysical properties [23,24] and geometric dimensions of the thermowell and the pipe

	Water pipe from FWH to EC	Water pipe from BIF* to ATMP
Density of pipe, ρ_{TW}	$7900\ kg/m^3$	$7900\ kg/m^3$
Heat capacity of pipe, C_{TW}	$460\ J/kgK$	$460\ J/kgK$
Thermal conductivity, k	$k_P = 28.2\ W/mK$	$k_P = 28.2\ W/mK$
Outer diameter, D_o	$55\ cm$	$15cm$
Inner diameter, D_i	$40\ cm$	$10\ cm$
Distance, L	$120\ m$	$100\ m$
Representative heat transfer coefficient, h	$\approx 13000\ W/m^2k$	$\approx 8000\ W/m^2k$
Biot number, Bi**	34	13
Representative effective heat transfer coefficient, h_{eff}	$\approx 550\ W/m^2k$	$\approx 2500\ W/m^2k$
Representative fluid velocity, u	$\approx 3.5\ m/s$	$\approx 1.2\ m/s$
Flow time delay, $t_{delay}\ (= L/u)$	$\approx 0.5\ min$	$\approx 1.5\ min$

* the location bifurcated to the 1st and 2nd attemperators, ** based on h, *** based on h_{eff}

Figure 7 shows the spray water flow recalculated from the enthalpy balance using the fluid and pipe transient (FPT) analysis, as well as the thermowell transient (TT) analysis. In Figure 7(a), the temperatures of the spray water injected into the 2nd attemperators (*Tw,ATMP*#2,*cal*, shown in red) was obtained using Eqs. (9) and (10) and the temperatures measured at the feedwater heater outlet (*TTW,w@FWH*, shown in a grey line). Here, the spray water from the feedwater heater was divided into the 1st and 2nd attemperator at a relatively short distance, while the distance from this bifurcation (BIF) point to the attemperators (ATMP) reached 100m (see Figure 4 and Table 1). Thus, the FPT analysis was applied only from BIF to ATMP and it was assumed that the fluid temperature at BIF (*Tw,BIF*) was the same as *TTW,w@FWH*. Here, the thermal time constant the for the pipe wall (τ_p ~ 3 min) and the time delay of flow (*tdelay* ~ 1.5 min) are comparable, thus the pipe temperature at BIF (*TP,BIF,cal* where x = 0 m, shown in dark blue), responds relatively quickly to the increase of the water temperature measured at FHW (*TTW,w@FWH*). This implies that the heat transfer from the water to the pipe is also significant and that the water temperature decreases significantly when flowing from BIF to ATMP. Thus, the calculated temperature of the spray water injected into the 2nd ATMP (*Tw,ATMP*#2,*cal*) was about 10 ˚C lower than the water temperature measured at FWH (*TTW,w@FWH*) during changing load operations. Likewise, the pipe temperature from BIF to ATMP also changed significantly. The pipe temperature at the 2nd ATMP (*TP,ATMP*#2,*cal*, shown in bright blue) was also about 10 ℃ lower than *TP,BIF,cal*. The results of the 1st attemperator in Figure 7(b) also show an almost identical trend to Figure 7(a), except that the temperature difference between *TTW,w@FWH* and *Tw,ATMP*#1,*cal* is as large as 20 ˚C during the first load changing operation. This is because during the first load changing operation, the spray flow rate of the 1st ATMP (*mw@ATMP*#1) was especially small, as shown in Figure 7(d).

Using the calculated temperatures of the spray water injected into the ATMPs (*T*w,*ATMP*#2,*cal* and *Tw,ATMP*#1,*cal*) instead of *TTW,w@FWH*, the spray water flows of the 2nd and 1st ATMPs were obtained and are shown as the red lines in Figure 7(c and d). Here, the calculated steam temperatures in Figs. 8(a and b) were used.

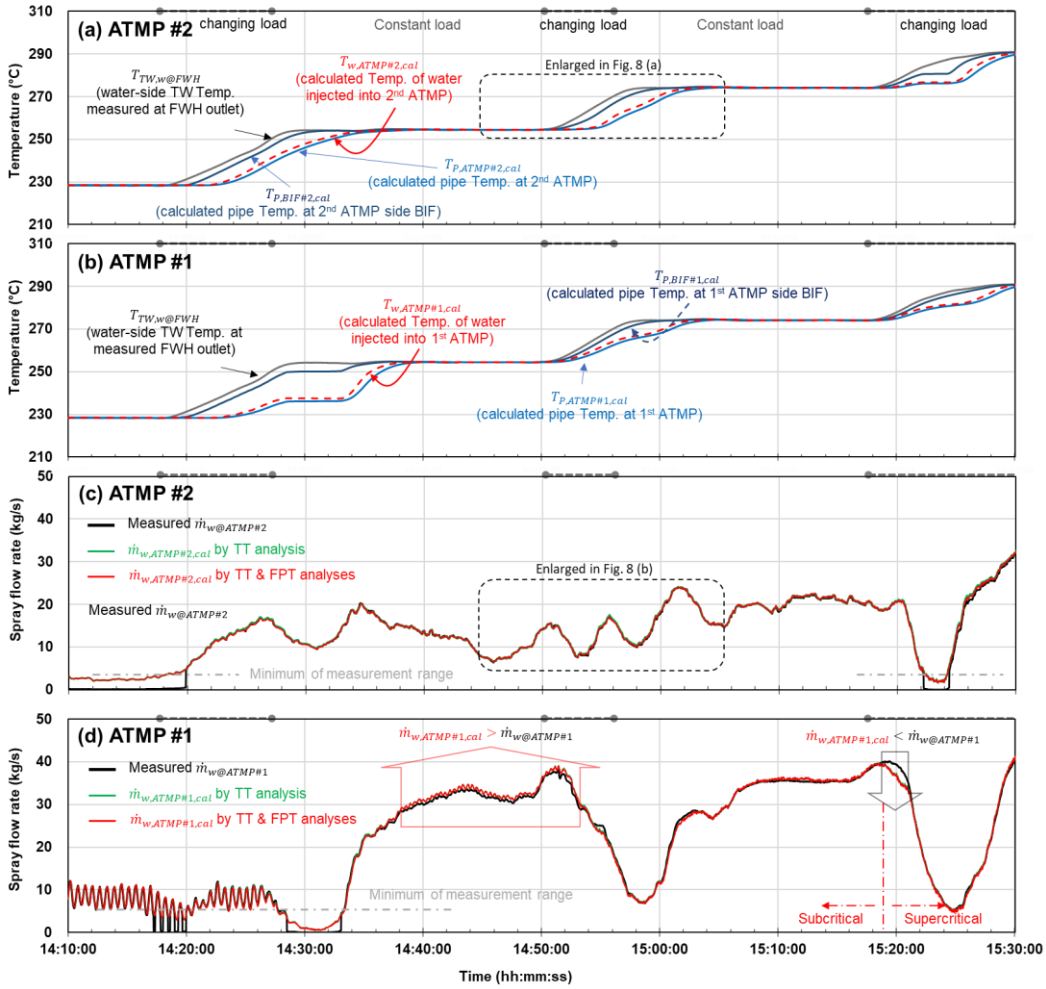

Figure 7 The results of a fluid and pipe transient analysis using the same loading commissioning data for the 1st and 2nd attemperators (ATMP). (a) The water temperature measured at the FWH outlet (black), the calculated pipe temperatures at the BIF of the 2nd ATMP (dark blue) and at the 2nd ATMP (bright blue) and the calculated temperature of the spray water injected into the 2nd ATMP (red), (b) those for the 1st ATMP, (c) the measured total (both A and B sides) spray water flow rate (black) and the calculated value for the 2nd ATMP by TT analysis (green) and by both TT and FPT analyses (red) (d) those for the 1st ATMP. (For interpretation of the references to color in this figure legend, the reader is referred to the web version of this article.)

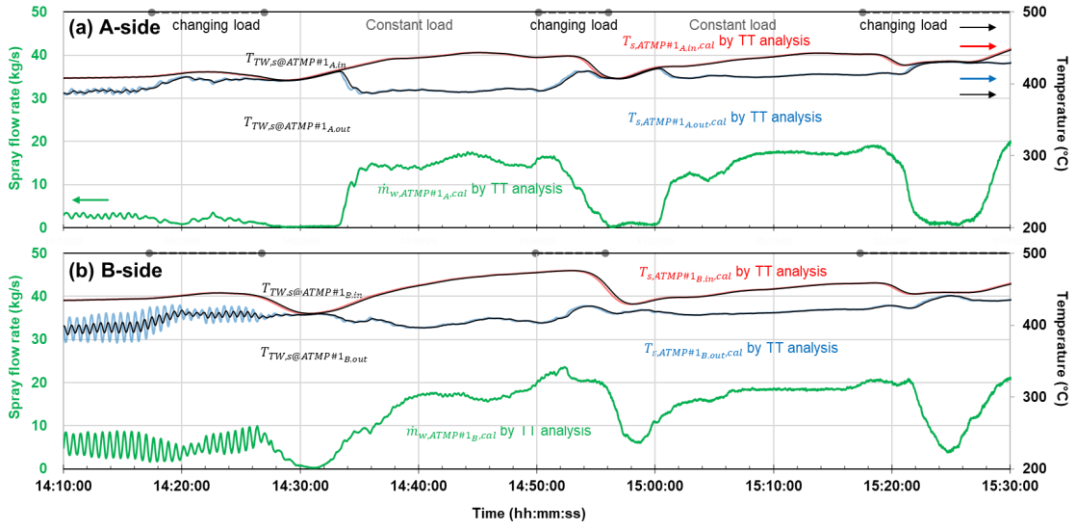

Figure 8 The results of the thermowell transient analysis. (a) The temperatures measured by the inlet and the outlet thermowells in the A-side attemperator and the respective steam temperature calculated using transient analysis (red and blue),and the spray water flow rate for the A-side attemperator obtained by using the calculated steam temperatures(green), (b)those for the B-side attemperator

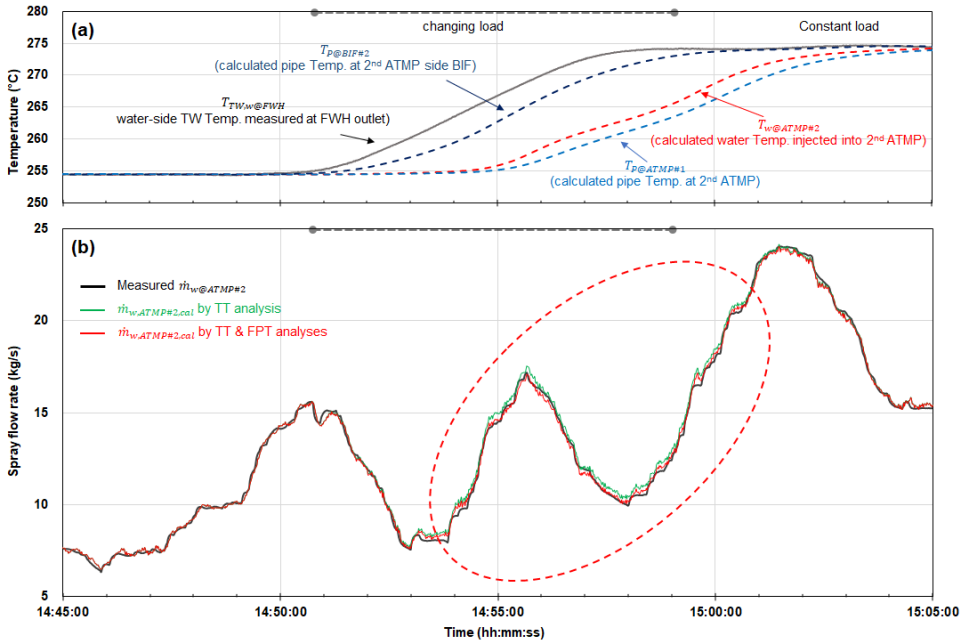

Figure 9 Enlarged views of (a) Figure7 (a) and (b) Figure7 (c)

Since the steam flow rate (ms,in) was approximately 10 times larger than the spray water flow rate, the change of about 10 ˚C in the spray water temperature did not make significant differences to Eq. (1). Therefore, the FPT analysis did not significantly change the calculated spray flow rate and the results obtained from the FPT (shown in red) and the TT analysis appear to be almost identical to those obtained with only the TT analysis (shown in green). However, as can be seen in the enlarged view in Figure 9(b), the FPT analysis improves the agreement between the calculated spray flow rate and the measured one during the load change and at later periods, which again verifies the validity of the FPT analysis.

Figure 9 compares the root mean square (RMS) values of the difference between the measured spray water flow rate and the calculated value using different analysis methods. Here, the spray flow rates in the 2nd attemperator (Figure 7(c)) were used, since they were in better agreement. The TT analysis significantly improves the accuracy of the calculated spray water flow rate calculated using the SS analysis. The FPT analysis can also further improve the accuracy. To confirm the reliability of the above results, additional de-loading commissioning data was analyzed using the transient analysis (TT and FPT analyses) and the results are shown in Figs. 15 and 16. Consistent with the results in Figure 7, the calculated spray water flow rate in the 2nd attemperator was in good agreement with the measured one, while the discrepancies could often be observed in the 1st attemperator.

Usually, the downstream temperature (outlet temperature) is compared for the validation of attemperator simulation [25]. However, in the case of not completely evaporated in attemperator system, comparing outlet temperature is not good enough for the validation because of thermal mass of thermowell and pipe (also, the reason is shown in chapter 2).

For above reason, this study uses the completion of the droplet evaporation as a validation factor. Therefore, the transient analysis studies carried out in this chapter will be compared to the simulation results in chapter 4, so that the reliability of the simulation will be increased.

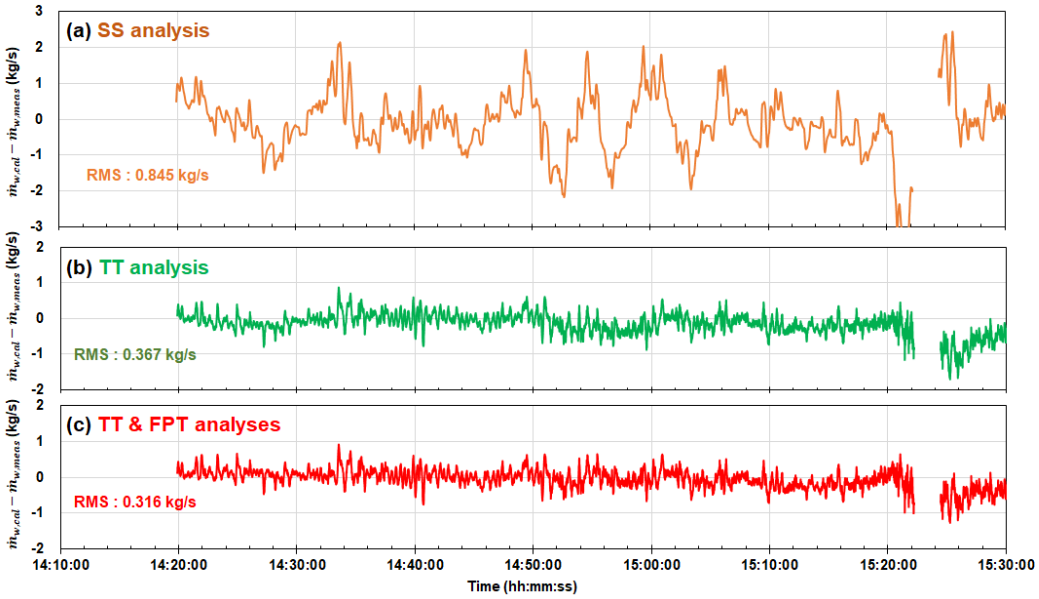

Figure 10 Root mean square (RMS) values of the difference between the measured spray water flow rate and the calculated values using different analyses. The data in Figure 7(c) (the loading commissioning data from the 2nd attemperator) was used. (a) steady-state (SS) analysis, (b) thermowell transient (TT) analysis, (c) fluid and pipe transient (FPT) analysis combined with the thermowell (TT) analysis.

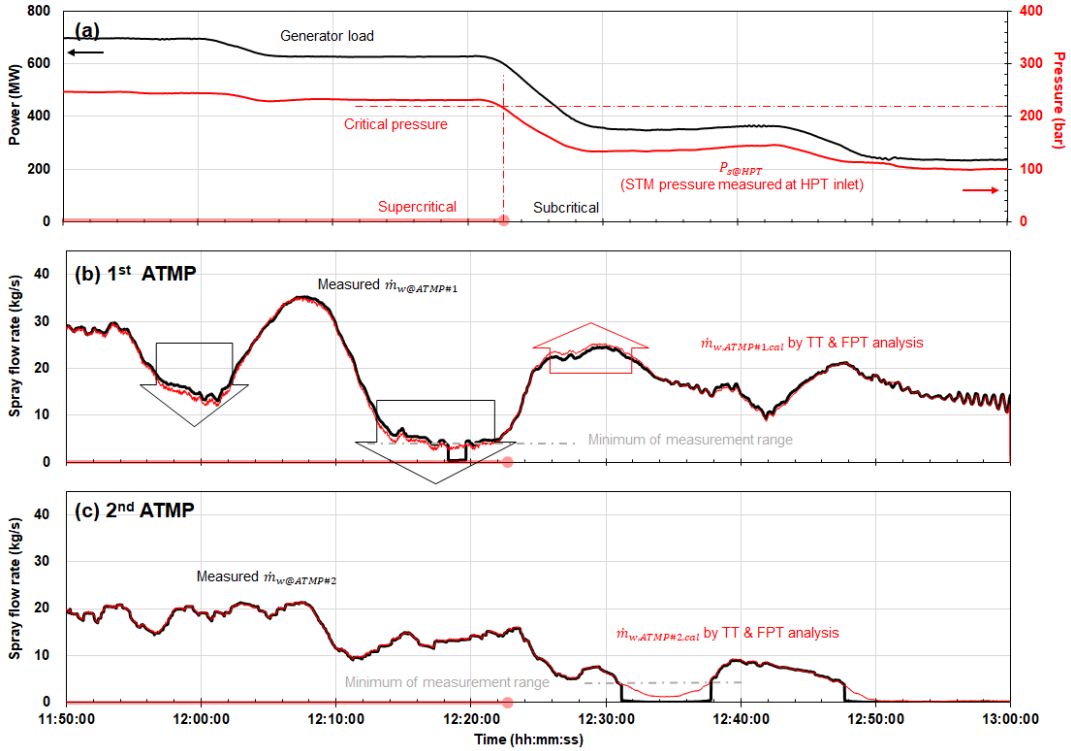

Figure 11 The results of a transient analysis of the de-loading commissioning data for the 1st and 2nd attemperators. (a) The generator load (black) and the steam pressure measured at the HPT inlet (red), (b) the measured total (both A and B sides) spray water flow rate (back) and the calculated value (red) for the 1st attemperator and (c) those for the 2nd attemperator.

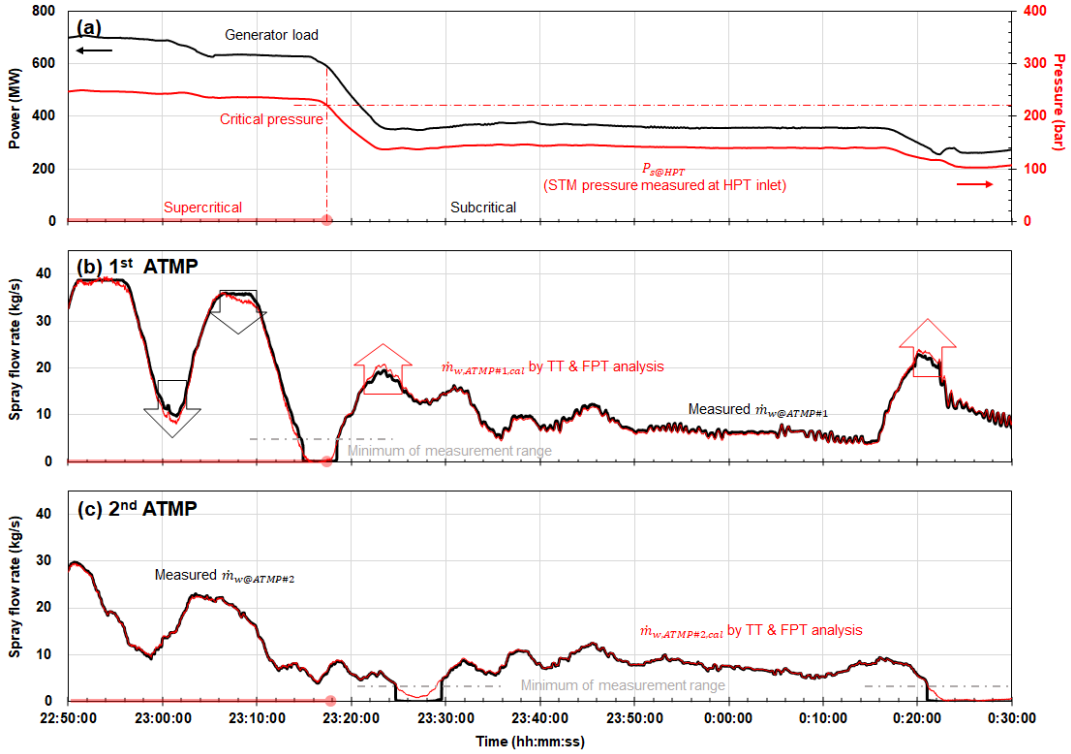

Figure 12 The results of a transient analysis of the de-loading commissioning data for the 1st and 2nd attemperators. (a) The generator load (black) and the steam pressure measured at the HPT inlet (red), (b) the measured total (both A and B sides) spray water flow rate (back) and the calculated value (red) for the 1st attemperator and (c) those for the 2nd attemperator.

CHAPTER 3. SIMULATION

In this chapter, the method of three-dimensional simulation of attemperator system is presented. The simulation domain is shown in Figure 13 which shows a representative attemperator system with a single nozzle and a venturi liner (also called thermal sleeve).

The important physics method used in simulation will be discussed in section 3.1 and the grid test will be explained in section 3.2.

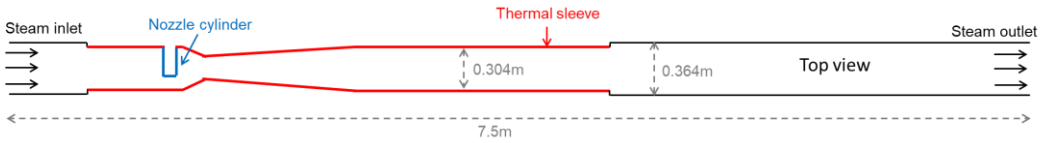

Figure 13 Top view of simulation domain

3.1 Numerical model description

3.1.1 Continuous phase flow

The Reynolds-averaged Navier-Stokes (RANS) approach with Lagrangian particle tracking is used to simulate the steam flow (continuous phase flow) and the behavior of droplets (dispersed phase flow). Here, the Mach number of the steam flow is lower than 0.3; thus, the mass conservation (Eq. (11)) and momentum (Eq. (12)) equations of the steam flow are calculated as Eulerian approach using the SIMPLE method that is valid for incompressible flow [26,27].

$$\frac{\partial \rho_s}{\partial t} + \nabla \cdot \left(\rho_s \vec{V}_s\right) = S, \tag{11}$$

$$\rho_s \frac{D\vec{V}_s}{Dt} = -\nabla p + \nabla \cdot (\bar{\tau}) + \rho_s \vec{g} + \vec{F}, \tag{12}$$

where ρ_s and $\vec{V}_s$ are the density and velocity of the steam respectively; p is the pressure; $\bar{\tau}$ is the stress tensor, $\vec{g}$ is gravity; and $\vec{F}$ is other external force.

In the current attemperator system, most of the droplets break up and evaporate in the

central region of the thermal liner. Thus, the k-ε turbulence model suitable for free-shear flow is used for the RANS equation of Eq. (12). It is noted that the k-ω model is known to perform better at adverse pressure gradients, near-wall boundary layers, and low Reynolds numbers.

3.1.2 Dispersed phase flow

A discrete phase model (DPM) is used for the dispersed phase flow of droplets in a Lagrangian reference frame. An alternative is the volume of fluid (VOF) model that tracks the interface between the gas and liquid phases; it is widely used to model free surfaces with high volume fractions of liquids [28–31]. However, in the attemperator system, the number of droplets is large, and the volume fraction of the droplets (dispersed phase) is less than 5%. Thus, the DPM model is used.

The discretization of the governing equations (Eqs. (11) and (12)) for the steam and the Lagrangian tracking of the droplets occurs in the same meshes. Furthermore, the mass, momentum, and heat exchanges between the steam and the droplets only occur inside the mesh, where the droplet is located.

The droplet acceleration ($d\vec{V}_d/dt$) was calculated using the drag force ($\vec{F}_{drag}$) and the gravity force ($\vec{F}_{gravity}$), for which the spherical drag coefficient defined by Morsi and Alexander [32] was used.

$$\rho_d \frac{d\vec{V}_d}{dt} = \vec{F}_{drag} + \vec{F}_{gravity}. \tag{13}$$

The heat transfer between the droplets and steam is balanced by the change in the sensible heat capacity of the droplet and latent heat of the droplet evaporation, as shown in Eq. (14). Subsequently, the amount of droplet evaporation becomes the source term (S) in the steam continuity equation (Eq. (11)).

$$hA_d(T_s - T_d) = m_d c_p \frac{dT_d}{dt} + \frac{dm_d}{dt} h_{fg}, \tag{14}$$

where m_d, c_p, and h_{fg} are the droplet mass, heat capacity, and latent heat, respectively; T is the temperature; h is the heat transfer coefficient; and h_{fg} is the latent heat of droplet.

In general, a fine mesh is preferred to accurately simulate steam flow. However, in the DPM, the solution of the steam continuity equation can diverge if the mesh size is too small, as droplet evaporation becomes the source term in the steam continuity equation (Eq. (11)) [33,34]. This phenomenon is discussed in further detail in Section 3.2.

3.1.3 Primary and secondary breakup model

Primary breakup occurs when the liquid jet is ejected from the nozzle, and it determines the initial droplet size distribution. This distribution is assumed to be a Rosin–Rammler distribution [35,36] that is expressed by a representative droplet size (Sauter mean diameter, d_{32}) and a spread parameter. Herein, d_{32} was calculated from the Weber number (We) using the correlation proposed by Wu et al. (Eq. (1)) and the spread parameter for non-cavitating flow [37].

$$d_{32} = 133.0\lambda We^{-0.74} \qquad \text{where, } We \equiv \frac{\rho_d u^2 \lambda}{\sigma} \quad . \qquad (15)$$

Here, λ is the radial integral length scale at the jet exit, and ρ_d, u, and σ are the droplet density, velocity difference between the steam and droplets, and droplet surface tension, respectively.

The secondary breakup occurs due to the drag force on the droplets generated by the velocity difference between the droplets and steam. To model this phenomenon, CFD simulations of the droplet breakup use various approaches, generally based on either Taylor analogy breakup (TAB) or wave breakup model. The TAB model [38,39] uses spring-mass system analogies to describe the droplet breakup process caused by surface tension, droplet drag, and droplet viscous force, which is applicable for systems with a low Weber number. In contrast, the wave breakup model [15] is based on the Kelvin-Helmholtz instability and is valid for large Weber numbers (We>100) as in the case of the attemperator. Thus, the wave breakup model is used in this study.

It is noted that a significant factor that affects droplet evaporation life-time or distance is the size reduction due to droplet breakup [12–14], which is affected by the steam velocity field in the attemperator. Related to this, this study demonstrates the significant difference between a venturi-type and straight thermal liner, which is detailed in Section 5.2.

3.1.4 Interaction between wall and droplets

According to Stanton [40], the droplet behavior after impacting the wall can be divided into four regimes (splash, spread, stick, and rebound) as shown in Figure 14. The regimes are determined by the impact energies of the droplets (E) (given by Eq. (16)) and the wall temperature (T_w).

$$E^2 = \frac{\rho_d V_n^2 d_d}{\sigma}\left(\frac{1}{min(h_0/d_d,1)+\delta_{bl}/d_d}\right) \tag{16}$$

$$\delta_{bl} = \frac{d_d}{\sqrt{Re}} \qquad \text{where,} \quad Re = \frac{\rho_d V_n d_d}{\mu}$$

V_n and d_d are the droplet normal velocity to the wall and the droplet diameter, respectively; h_0 is the thickness of the water film on the wall; and δ_{bl} is the height of the boundary layer.

Herein, the wall temperature (T_w) is close to the steam temperature (T_s), which is higher than the saturation temperature ($\therefore\ T_w \gg T_{crit} \approx T_{sat}$). The impact energies ($E$) of most of the droplets were under E_{crit} (≈ 57.7). Therefore, the rebound model was adopted herein.

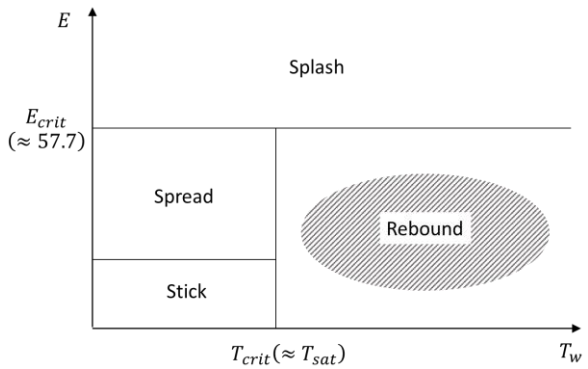

Figure 14 Wall interaction criterion chart [40]. The dashed area indicates the regime adopted herein.

3.1.5 Radiation effect

Since the droplet is small compared to the pipe the system can be considered as small convex object in a large cavity system in radiation. In this case the view factor of droplet to wall becomes 1 ($F_{12} = 1$). Therefore, the radiation heat flux to the droplet can be expressed as follows,

$$q'' = \alpha_{water}\sigma {T_w}^4 - \varepsilon_{water} {T_{drop}}^4 \quad (17)$$

From the Wien's displacement law, the most dominant wavelength of wall temperature and droplet temperature is $\lambda = 4.28\mu m$ and $\lambda = 5.04\mu m$ respectively. Therefore, since the absorption length is much smaller than the droplet size, the transmissivity can be assumed to be zero. This study is an enclosed case and can be assumed to have the same absorptivity and emissivity. From the transmissivity, the absorptivity and emissivity of water can be regarded as 1. The Eq. 17 can be simplified as follows,

$$q'' = \sigma\varepsilon_{water}\left({T_w}^4 - {T_{drop}}^4\right) \quad (18)$$

In the other hand, the convective heat flux can be expressed as follows,

$$q'' = h\left(T_w - T_{drop}\right) \quad (19)$$

Using the representative operating conditions in attemperator system, the radiative flux is $6{,}742\ W/m^2$ and the convective heat flux is $407{,}000\ W/m^2$. Compare the effect of radiation to the convection, the radiative heat flux is less than 2% of convective heat flux. Therefore, the radiation effect is neglected in this study.

3.1.6 Droplet collision

The dilute flow is defined when the volume fraction of particles is smaller than 0.0005 [41]. In the attemperator system, the volume fraction of sprayed water to steam flow is about 0.005 which stands for the dense flow. Therefore, the droplet collision model of O'Rourke is used [42].

3.2 Grid test

The mesh was generated using the ICEM software package provided by ANSYS. Most of the flow domain was created using hexa meshes owing to their high orthogonal quality and low skewness value. In particular, the domain adjacent to the nozzle cylinder was also created using hexa meshes to accurately simulate the boundary layer effect. In contrast, as the nozzle cylinder is perpendicular to the direction of steam flow (Figure 13), tetra meshes were generated in region 2. The overall mesh shape used in the simulation domain is shown in Figure 15.

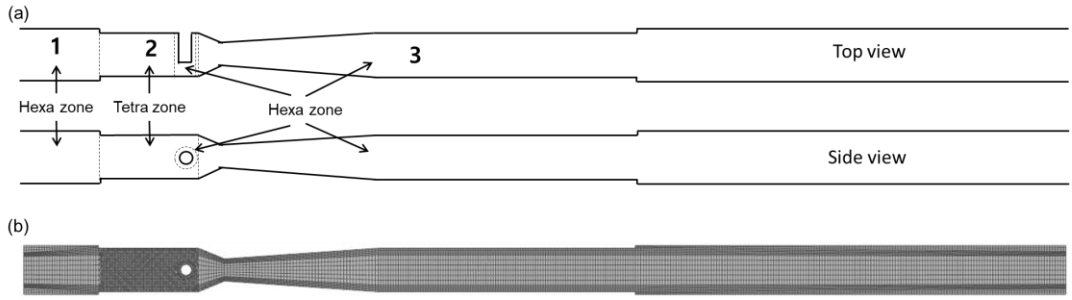

Figure 15 (a) composition of mesh shape; and (b) overall mesh shape in the simulation domain.

3.2.1 Grid dependency test

The simulation was performed using ANSYS Fluent 19.1, and the velocity and pressure fields were solved using the k- ε turbulence model and the SIMPLE method [35]. Grid dependency tests were performed by varying the total number of meshes (3 million, 1 million, 0.16 million, 0.05 million, and 0.02 million) and the resulting velocity contours are shown in Figure 16(a). Droplet evaporation is significantly affected by the droplet size, which in turn is affected by the droplet breakup that occurs due to the velocity difference between the droplets and the steam. Consequently, the steam velocity profiles at the center, as shown in Figure 16(b), were compared in the grid dependency test. As shown in the dotted area in Figure 16(b), the velocity profiles with 3 million, 1 million, and 0.16 million meshes were similar, whereas those with 0.05 million and 0.02 million meshes were relatively small. Therefore, considering the computational costs and accuracy, a total of 0.16 million meshes

was determined to have suitably passed the grid dependency test for steam flow (Table 2).

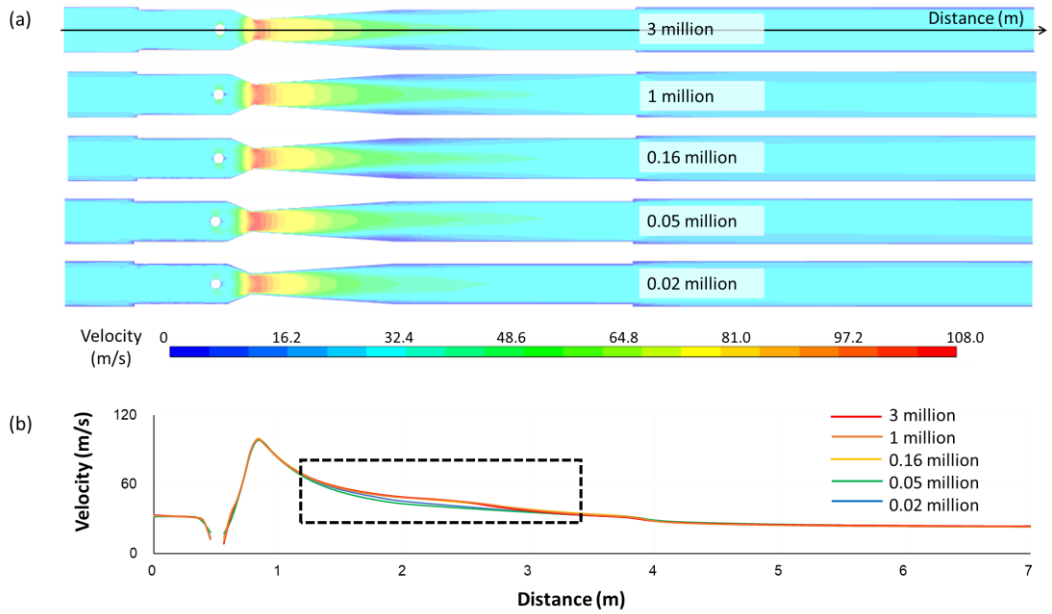

Figure 16 Grid dependency test of steam flow: (a) velocity contour and (b) graph of the center line velocity with different numbers of meshes.

3.2.2 Grid divergence test

In addition, we performed a grid convergence test considering droplet evaporation. As mentioned in Eqs. (13) and (14), droplet evaporation is the source in the steam continuity equation. Therefore, if the mesh in the DPM is too small, the steam velocity can become abnormally large owing to droplet evaporation. Figure 17 illustrates the simulation result with 1 million meshes. As shown, the steam velocity in the attemperator is approximately 100–200 m/s, but the velocity behind the nozzle cylinder is approximately 700 m/s, which is abnormal. This confirms that 1 million meshes results in divergence.

Table 2 summarizes the results of the grid dependency and grid convergence tests of the velocity and droplet evaporation, respectively. Based on these results, the simulation herein

was performed using 0.16 million meshes.

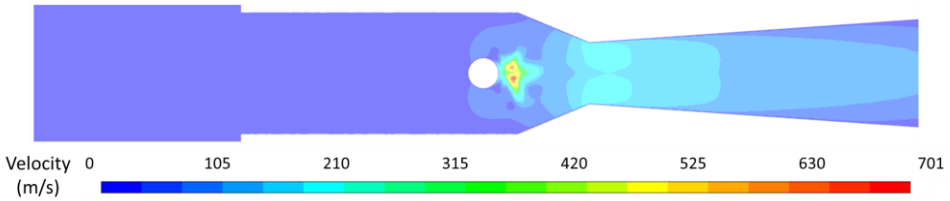

Figure 17 Example of velocity divergence owing to droplet evaporation (1 million meshes).

Table 3 Results of grid dependency and grid convergence tests

Number of meshes	3 million	1 million	0.16 million	0.05 million	0.02 million
Velocity	passed	passed	passed	-	-
Droplet evaporation	diverging	diverging	converging	converging	converging

3.3 Feasibility of evaporation model

The mass flux at the surface can be expressed as

$$\dot{m}''_{1,s} = -\frac{\rho_l}{4\pi r_s^2}\frac{d}{dt}\left(\frac{4}{3}\pi r_s^3\right) = -\rho_l \frac{dr_s}{dt} \tag{20}$$

After integration and expressing the result in terms of diameter, so called d squared evaporation law is expressed as following,

$$d_s^2 = d_{s,0}^2 - \left[8\rho_s \alpha_s \frac{c_p(T_{steam} - T_{droplet})}{\rho_l h_{fg}}\right] \tag{21}$$

To show the feasibility of evaporation model, the Eq. 21 and the simulation results are compared and shown in Figure 18.

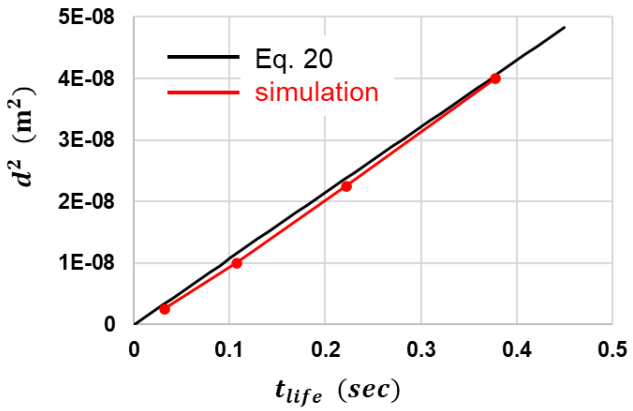

Figure 18 The results of evaporation simulation compared to Eq. 20

CHAPTER 4. VALIDATION OF NUMERICAL SIMULATION

In a previous study (chapter 2), the commissioning operation data of an attemperator were analyzed using transient thermal analysis based on the enthalpy balance method. The results of this analysis can be used to determine whether the sprayed droplets evaporate completely before reaching the thermowell, considering the four cases listed in Table 3. The water droplets completely evaporated before reaching the thermowell in Cases 3 and 4, but failed to do so in Cases 1 and 2. This is because compared to Cases 3 and 4, Cases 1 and 2 exhibited relatively weak droplet breakup owing to a lower steam mass flow rate (i.e., lower steam velocity). In addition, the heat capacity of the flowing steam that was available for the evaporation of the sprayed water droplets was low in Cases 1 and 2. We simulated the four cases listed in Table 3 and compared the simulation results with the transient thermal analysis results to validate the numerical method developed herein. Table 4 lists the basic geometrical parameters of the representative attemperator studied herein.

Table 4 Operating conditions of selected cases from the transient analysis of commissioning data [7]

	Operating pressure	Steam		Spray		Results from commissioning data [7]
		$\dot{m}_s$	T_s	$\dot{m}_{water}$	T_{water}	
Case 1	11 MPa	93 kg/s	430 °C	9.0 kg/s	246 °C	Not evaporated within 6.1 m
Case 2*	12 MPa	99 kg/s	437 °C	10.3 kg/s	249 °C	Not evaporated within 6.1 m
Case 3	14 MPa	143 kg/s	443 °C	6.3 kg/s	252 °C	Completely evaporated within 6.1 m
Case 4	15 MPa	146 kg/s	466 °C	10.2 kg/s	249 °C	Completely evaporated within 6.1 m
Simulations in Section 4	11 MPa	93 kg/s	430 °C	2 kg/s	246 °C	

* The calculation time for Case 2 was approximately 28 days using 40 cores of a Xeon Gold 6148 CPU.

Table 5 Major geometric information of the representative attemperator

Nozzle hole diameter	Nozzle cylinder diameter	Main pipe diameter	Thermal liner diameter	Diameter at the venturi neck	Thermowell distance from the nozzle cylinder
40 mm	80mm	364 mm	304mm	175mm	6.1 m

4.1 Simulation results of cases 1 and 2 (incomplete evaporation)

Figure 18 shows the simulation results of Case 1. In Figure 18(a), the average inlet steam velocity (21 m/s) accelerated to 108 m/s at the venturi neck (displayed in red in Figure 18(a)), and then gradually decreased. As shown in Figure 18(b), water was sprayed at a temperature of 246 °C, and the steam was desuperheated from approximately 430 °C to 375–396 °C at the attemperator outlet. As shown, the flow direction and temperature contour of the steam were inclined to one side owing to the asymmetric shape of the nozzle cylinder. Figs. 18(c)–18(f) show the scatter plots of the droplet position, diameter, velocity, and temperature, respectively, with the increase in the distance from the nozzle. The red and yellow dots represent the droplets that were larger and smaller than 50 μm, respectively. The same color scheme is used to represent these droplet sizes in subsequent figures. As shown in Figure 18(c), the droplets lean to one side inside the thermal liner. As shown in Figure 18(d), the large droplets were broken down into smaller droplets as they passed through the venturi region. As shown in Figure 18(e), the small droplets accelerated relatively well from the jet velocity (8.8 m/s) to the maximum steam velocity (indicated by the black line) owing to their small inertia, whereas the large droplets did not accelerate well. Figure 18(f) shows the temperature of the droplets. The temperature of the small droplets increased to the saturation temperature (T_{sat}) faster than that of the large droplets, and most droplets reached T_{sat} in a very short distance of ~0.3 m.

As shown in Figure 18(g), the mass flow rate of the nonevaporated water ($\dot{m}_{water}$) gradually decreased from the injected water flow rate (8.94 kg/s) owing to evaporation, which remained incomplete at the thermowell ($\dot{m}_{water}$ = 0.3 kg/s at the thermowell). This is consistent with the results in Figs. 18(c)–18(f), wherein the droplets are still present at the thermowell. It should be noted that Figs. 18(c)–18(g) were obtained from the post-processing particle tracking data of the ANSYS Fluent simulations using a custom MATLAB code.

Figure 19 presents the simulation results of Case 2. The steam mass flow and steam temperature in this case were slightly higher than those in Case 1, which can result in faster evaporation. However, these differences did not result in significant differences in the results

as more water was sprayed in Case 2. Therefore, as in Case 1, complete evaporation did not occur before the flow reached the thermowell, as shown in Figure 19.

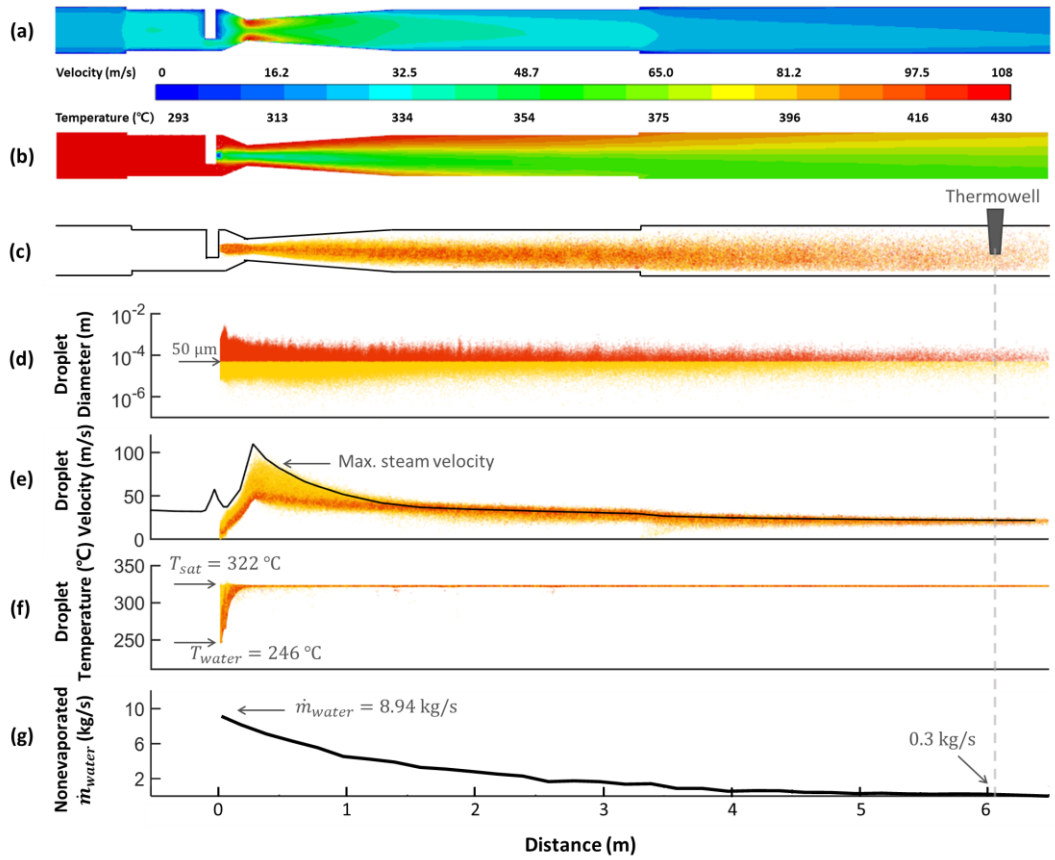

Figure 19 Simulation results of Case 1: (a) velocity contour of steam; (b) temperature contour of steam; (c) droplet position scatter plot (red and yellow dots indicate droplets that were larger and smaller than 50 μm, respectively); (d) droplet diameter scatter plot; (e) droplet velocity scatter plot (maximum steam velocity is indicated by a black line); (f) droplet temperature scatter plot; and (g) mass flow rate of nonevaporated water. Figs. 7(c)–7(g) were obtained from the post-processing particle tracking data obtained from ANSYS Fluent simulations using custom MATLAB code.

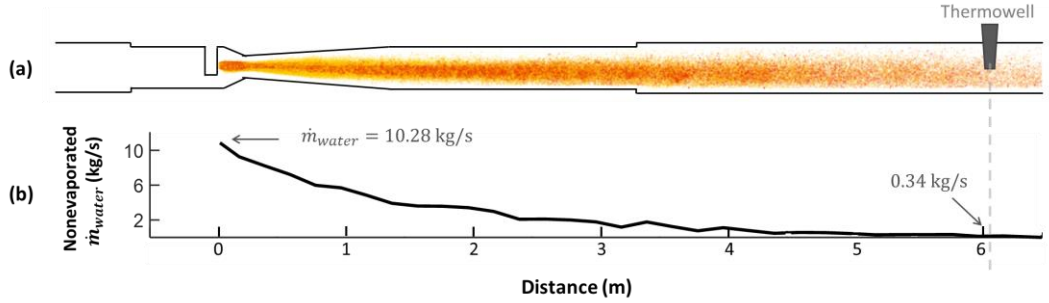

Figure 20 Simulation results of Case 2: (a) droplet position scatter plot (red and yellow dots indicate droplets that were larger and smaller than 50 μm, respectively) and (b) mass flow rate of nonevaporated water

4.2 Simulation results of Cases 3 and 4 (complete evaporation)

Figure 20 presents the simulation results of Case 3. Although the steam velocity and temperature values are higher than those in Case 1, the overall trends of the steam velocity and temperature contours in Figs. 20(a) and 20(b) are similar to those in Figs. 18(a) and 18(b), respectively. As shown in Figs. 20(c)–20(g), the large droplets disappeared rapidly while passing through the venturi, which indicates that the breakup process was very strong. Consequently, the sprayed water completely evaporated within 2 m from the nozzle.

The simulation results of Case 4 are presented in Figure 21. In this case, although the sprayed water flow rate ($\dot{m}_w$) was almost twice as large as that in Case 3, complete evaporation occurred within 2.5 m from the nozzle.

In summary, the simulation results of the four cases are consistent with the transient thermal analysis results obtained from the commissioning data. That is to say, the simulation results also demonstrated that the water droplets completely evaporated before reaching the thermowell in Cases 3 and 4, but not in Cases 1 and 2. Therefore, the proposed simulation model can predict droplet breakup and evaporation in the attemperator with reasonable accuracy.

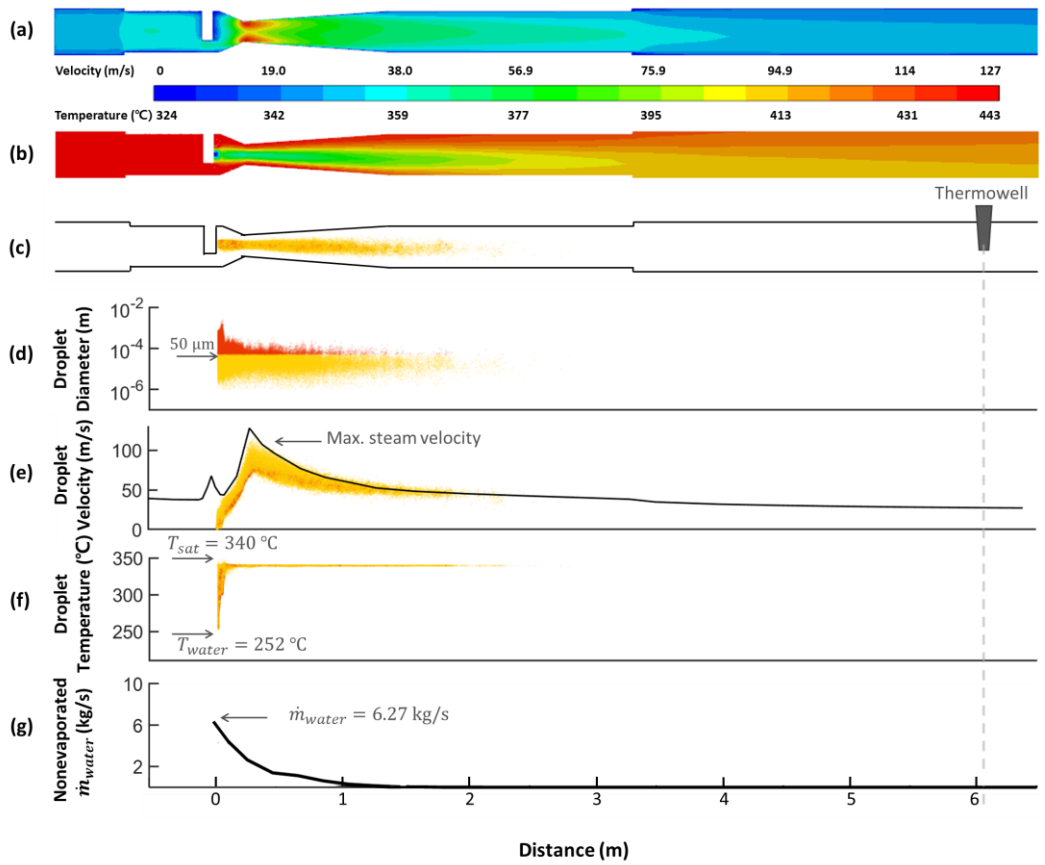

Figure 21 Simulation results of Case 3: (a) velocity contour of steam; (b) temperature contour of steam; (c) droplet position scatter plot; (d) droplet diameter scatter plot; (e) droplet velocity scatter plot; (f) droplet temperature scatter plot; and (g) mass flow rate of nonevaporated water.

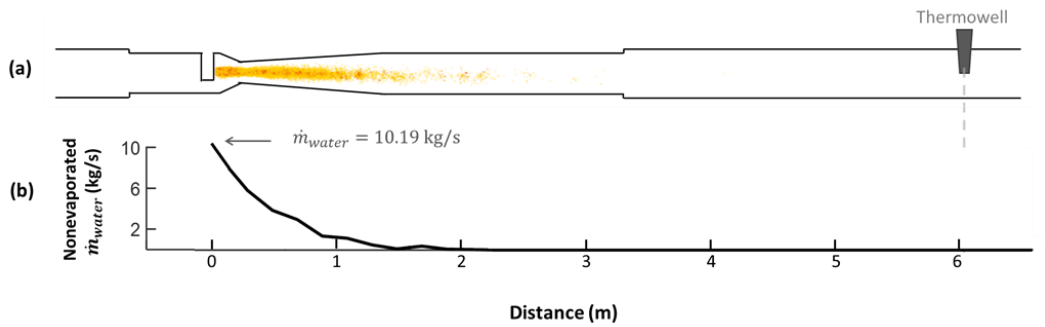

Figure 22 Simulation results of Case 4: (a) droplet position scatter plot and (b) mass flow rate of nonevaporated water.

CHAPTER 5. SIMULATION OF VARIOUS ATTEMPERATOR DESIGNS

The simulation results of various attemperator designs are presented in this section. The standard case comprises a single nozzle hole (40 mm diameter) and a venturi-type thermal liner as shown in Figure 22(a). The simulation results of this standard case are compared with those comprising a symmetric nozzle cylinder (Figure 22(b)), a straight thermal liner (Figure 22(c)), and multiple nozzles (Figure 22(d)). Table 5 summarizes the major geometric features of each design case.

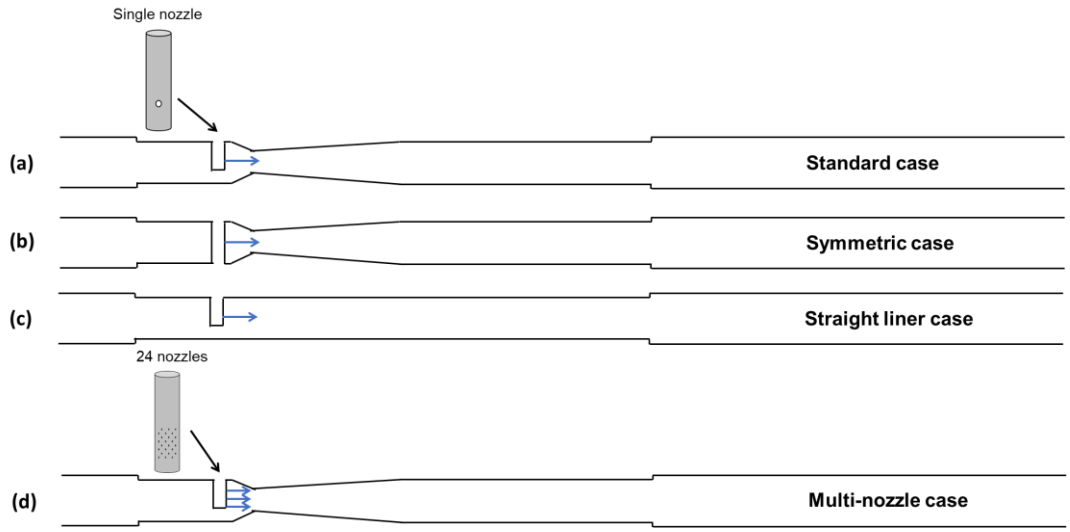

Figure 23 Attemperator schematics of the: (a) standard case; (b) symmetric case; (c) straight liner case; and (d) multi-nozzle case.

Table 6 Summary of the geometric differences in the attemperator designs

	Nozzle cylinder	Number of nozzle holes	Shape of liner
Standard case	Asymmetric	Single	Venturi
Symmetric case	Symmetric	Single	Venturi
Straight liner case	Asymmetric	Single	Straight
Multi-nozzle case	Asymmetric	Multiple (24 holes)	Venturi

5.1 Simulation results of the symmetric case

As discussed in Section 4.1, the asymmetric shape of the nozzle cylinder inside the main pipe tilts the steam flow to one side. This can increase the likelihood of the droplet impacting the wall of the thermal liner and the main pipe, which results in thermal stress. To resolve this problem, as shown in Figure 22(b), the nozzle cylinder was extended to the opposite wall of the thermal liner to make it symmetric.

The droplet position scatter plots of the standard and symmetric cases are shown in Figure 23(a). Owing to the symmetric geometry of the nozzle cylinder, the droplet leaning phenomena disappears. Other than that, the overall droplet breakup and evaporation trends are similar in both cases, and the mass flow rates of the nonevaporated water are also similar in both cases, as shown in Figure 23(b).

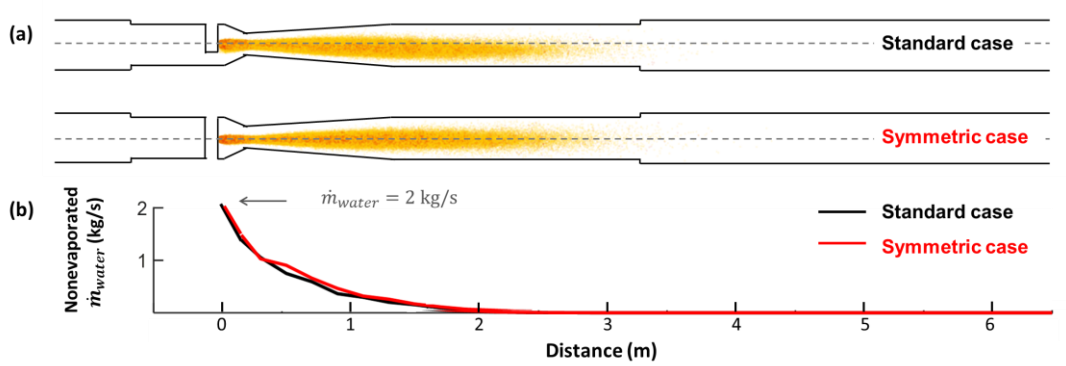

Figure 24 Comparison of simulation results of standard and symmetric cases: (a) droplet position scatter plots and (b) mass flow rates of nonevaporated water.

5.2 Simulation results of the straight liner case

In the standard case, the steam velocity increased significantly as it passed through the venturi section, which can enhance the secondary breakup of large droplets and increase the rate of evaporation. To evaluate the effectiveness of the venturi on secondary breakup, we performed simulations using a straight thermal liner.

Figure 24 compares the results of the standard and straight liner cases. In the straight liner case, droplet evaporation remained incomplete till the end (x = 6.5 m) of the simulation domain and several large droplets (indicated by red) were still present in the flow, as shown in Figure 24(a). The droplet diameter scatter plot (Figure 24(b)) also indicates the presence of several large droplets. This implies that the secondary breakup of large droplets was weak. The reason for this behavior can be explained by the droplet velocity scatter plot (Figure 24(c)). Secondary breakup is highly dependent on the difference in velocity between the droplets and the steam. In the standard case, the steam velocity accelerates significantly across the venturi. However, this does not happen in the straight liner case. Consequently, fewer large droplets break down into smaller droplets in the straight liner case, resulting in incomplete droplet evaporation (Figure 24(d)).

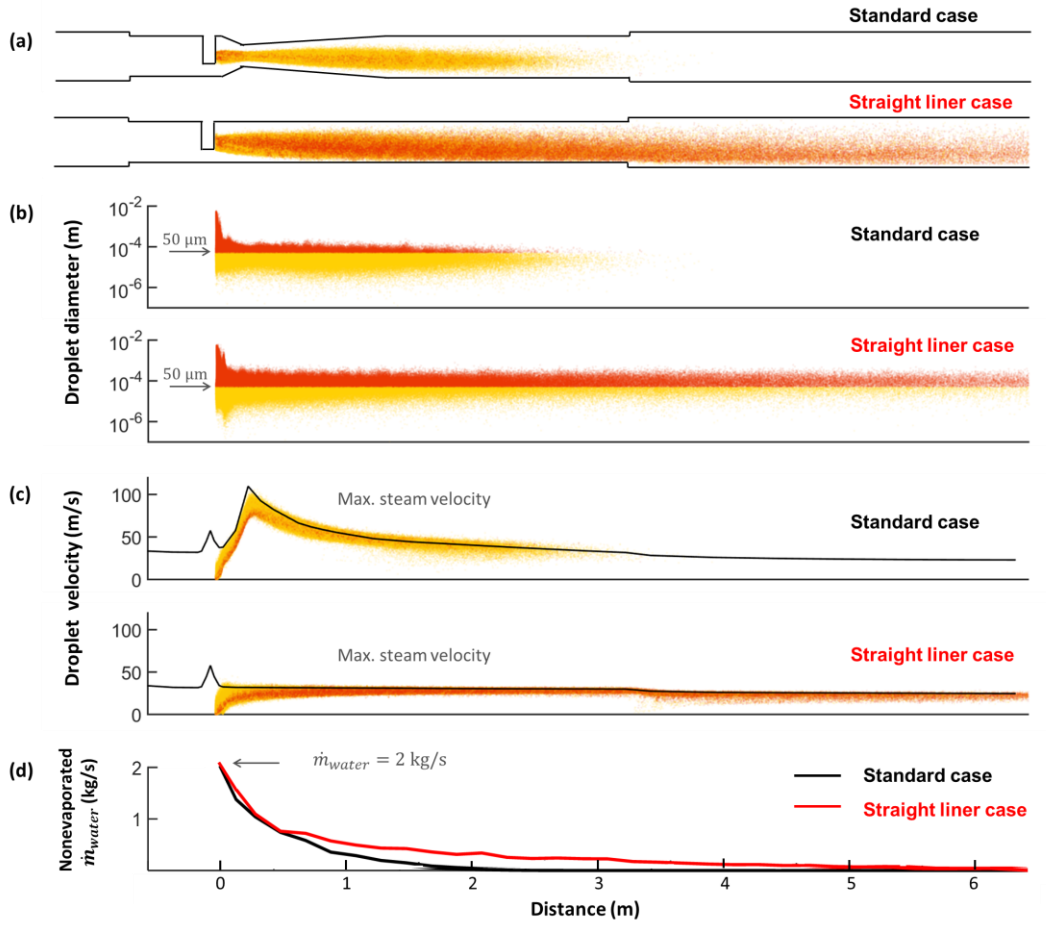

Figure 25 Comparison of the simulation results of the standard and straight liner cases: (a) droplet position scatter plots; (b) droplet diameter scatter plots; (c) droplet velocity scatter plots; and (d) mass flow rates of nonevaporated water.

5.3 Simulation results of the multi-nozzle case

As shown in Figure 22(d), in the multi-nozzle case, 24 holes with a diameter of 8 mm each were used to reduce the initial droplet size. Notably, the total area of the opening (≈ 1200 mm^2) was the same as that in the single nozzle (standard) case (40 mm diameter), to ensure the same initial injection speed of the water jet. The location of the multi-nozzle holes on the cylinder is shown in Figure 25(a).

As shown in Figure 25(a), in the multi-nozzle case, the droplets were distributed over a larger area after injection, and evaporated faster compared to the standard case. As shown in the droplet diameter scatter plots in Figure 25(b), the maximum initial droplet size distribution was significantly smaller in the multi-nozzle case compared to the standard case, and several very small droplets (indicated by the dotted circle in Figure 25(b)) were observed. These very small droplets evaporated rapidly and disappeared within a short distance (≈ 0.1 m) as they reached the saturation temperature quickly (e.g. Figure 20(f)).

As shown in Figure 25(c), the mass flow rate of the nonevaporated water decreased rapidly (i.e. the evaporation rate was much higher) in the multi-nozzle case compared to the standard case. This abrupt decrease primarily occurred because the initial droplet size distribution in the multi-nozzle case was significantly smaller than that in the standard case owing to the smaller nozzle hole size in the former, and secondary breakup produced even smaller droplets as they passed through the venturi.

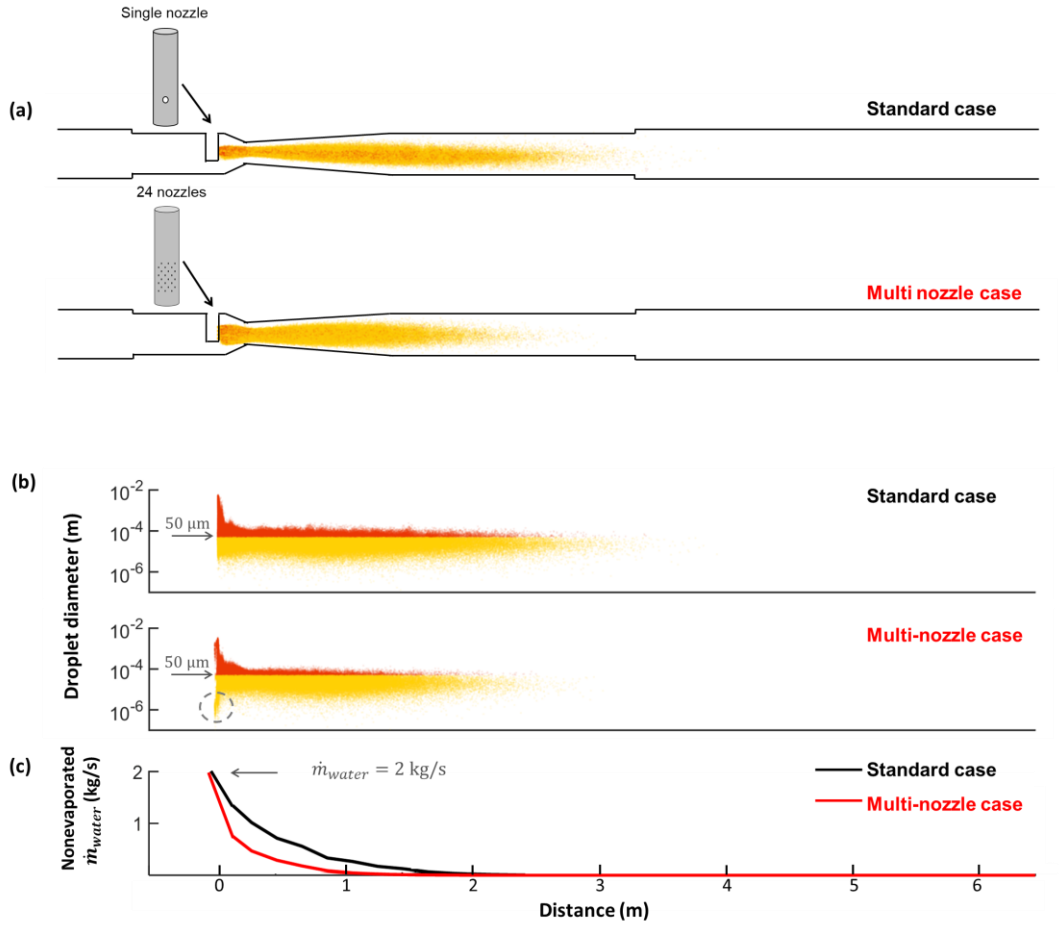

Figure 26 Comparison of the simulation results of the standard and multi-nozzle cases: (a) droplet position scatter plots; (b) droplet diameter scatter plots; and (c) mass flow rates of nonevaporated water.

5.4 Parametric study

In section 5.2, the venturi liner and straight liner cases are compared to analyze that the effect of venturi on evaporation. Therefore, in this section, the effect of venturi on evaporation will be discussed in detail by changing the diameter of venturi neck. The diameter of venturi neck is 165mm, 216.8mm and 323.9mm as shown in Figure 27(a).

Figure 27(b) shows the evaporation distance varying the venturi neck diameter (D) and nozzle diameter (d). When d is 40mm (black line), as the venturi neck diameter increases, the evaporation distance also increases. This is due to the droplet breakup induced by velocity difference between the steam and droplet.

As the venturi neck diameter (D) increases, the steam velocity change due to the venturi is small. Therefore, the evaporation distance of droplet is long because the large droplet remaining. These trends are similar in other nozzle diameter cases (20mm, 50mm) shown in Figure 27(b).

In 323.9mm case (which is straight liner case), 50mm nozzle diameter evaporates faster than 20mm diameter. However, in 165mm case, all sizes of nozzle diameter show similar evaporation distance (dotted line in Figure 27(b)). This indicates that since the venturi occur the secondary breakup, the effect of nozzle size become small.

The reason for the large nozzle diameter evaporates faster than small nozzle diameter is due to the injection velocity. Since the mass flow rate of sprayed water is same, the velocity is different varying the nozzle diameter. Each case of injection velocity is shown in Table 6. The case of 50mm nozzle diameter shows large velocity difference between the steam and droplet. Therefore, the 50mm nozzle diameter case evaporates faster than other two cases.

To analyze the effect of initial droplet size on evaporation, the nozzle area is fixed to make the injection velocity identical (Figure 28). The results are shown in Figure 29. Here, as the nozzle diameter become smaller, the evaporation distance is shorter. Since the small nozzle diameter sprays the small droplets, the surface-to-volume ratio becomes large, so that the droplet evaporates faster.

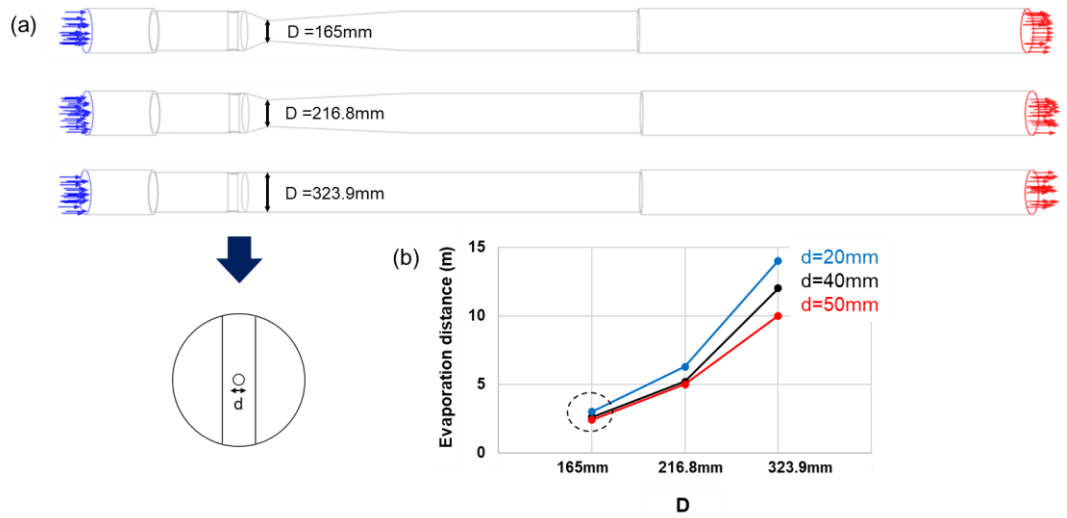

Figure 27 (a) Several type of venturi neck diameter; (b) results of evaporation distance varying the venturi and nozzle diameter

Table 7 Velocity of nozzle diameter (Figure 27)

	# of nozzle	Steam velocity	Water velocity
50 mm	1	27 m/s	1.25 m/s
40 mm			1.95 m/s
10 mm			31.3 m/s

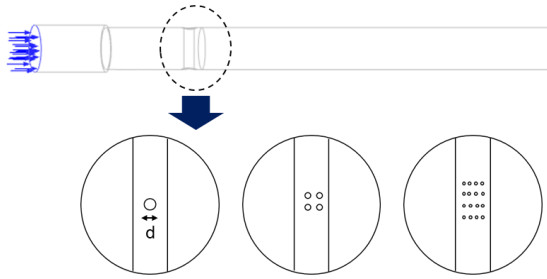

d	# of nozzle	Total nozzle area	Velocity
40mm	1	0.001257 m^2	1.958 m/s
20mm	4		
10mm	16		

Figure 28 Cases of varying nozzle diameter and number of nozzles

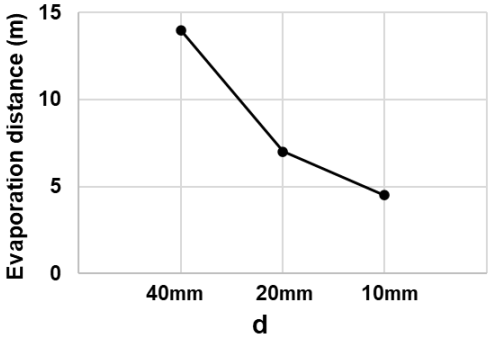

Figure 29 Evaporation distance varying the nozzle diameter

CHAPTER 6. DISCUSSION

In Chapter 2, to verify the complete desuperheating of the spray injected steam before reaching the outlet thermowell, spray water flow was calculated based on the enthalpy balance between the inlet and the outlet of the attemperator, and was compared to measured results.

Due to the large heat capacity of the thermowell, its measurement cannot respond to rapid changes of the steam temperature. In addition, the temperature of the spray water cannot be accurately represented by the temperature measured at the feedwater heater outlet far from the attemperator during changing load operations. Thus, the steady-state analysis using the enthalpies based on these measured temperatures could not accurately calculate the spray water flow.

To compensate for these two major errors, a transient analysis using a lumped capacitance model was carried out. Here, in both cases, Biot numbers were larger than 10, thus effective heat transfer coefficients were employed. Through the transient analysis, the steam temperatures at the inlet and the outlet of the attemperator and the temperature of the spray water injected into the attemperators could be estimated.

Using this data, the spray water flow could be calculated accurately enough to verify whether desuperheating of the spray injected steam was completed before reaching the outlet thermowell, even during changing load operation. Based on the results of the transient analysis of commissioning data (1 loading case and 2 de-loading cases), it could be verified that the distance from the spray nozzle to the outlet thermowell in the 2nd attemperators was sufficiently large to ensure the complete desuperheating of the spray injected steam, but this was not the case in the 1st attemperators. These results appear to be reasonable considering the superheat of the steam and the thermowell locations in the 1st and 2nd attemperators. In addition, when the spray injected steam was not completely desuperheated before reaching the outlet thermowell in the 1st attemperator, the thermowell measured a lower temperature than the completely desuperheated steam temperature under subcritical conditions and a

higher temperature under supercritical conditions. Note that the temperature reading of the outlet thermowell in the attemperator is one of the major inputs used in the feedback control of the spray water. Thus, the methodology presented here and its analysis results could be effectively used to revise the control logic to better adjust steam temperatures. In addition, these results provide useful information for future attemperator designs.

In three-dimensional simulation, the grid test was carried out in two ways: in the aspect of flow and evaporation. For the accuracy of steam velocity, finer grid is preferred. In contrast, the finer grid results diverging in droplet evaporation as explained in Chapter 3. Therefore, the grid was selected considering the satisfaction of both cases.

The simulation results indicate that multiples nozzles with a venturi thermal liner (Figs. 13 and 14) produce smaller droplets and reduce the evaporation distance. To quantitatively evaluate the effect of these design changes on the droplet breakup and evaporation processes, the variation in the droplet volume flow distribution ($\mathrm{d}Q/\mathrm{d}d$ ($m^3/s\cdot\mu m$)) (left-hand side) and the droplet number flow distribution ($\mathrm{d}(\#/s)/\mathrm{d}d$ ($\#/s\cdot\mu m$)) (right-hand side) with the droplet size were plotted at various distances from the nozzle, as shown in Figure 15.

As the lifetime of a droplet in quiescent air is proportional to its surface area, small droplets disappear rapidly due to evaporation. Therefore, the curve of $\mathrm{d}(\#/s)/\mathrm{d}d$ generally exhibits a right-skewed distribution with a peak value. However, if the strong breakup of large droplets occurs, the number of small droplets increases. Consequently, the curve of $\mathrm{d}(\#/s)/\mathrm{d}d$ can have a continuously decreasing distribution. In contrast, the curve of $\mathrm{d}Q/\mathrm{d}d$ always has a right-skewed distribution, as the droplet volume corresponds to the third power of the droplet diameter. Furthermore, the droplet size range where the value of $\mathrm{d}Q/\mathrm{d}d$ is significant is wider than that for $\mathrm{d}(\#/s)/\mathrm{d}d$. In addition, the integrated area of $\mathrm{d}Q/\mathrm{d}d$ corresponds to the mass flow rate of the nonevaporated water at the corresponding distance in Figs. 12(b), 13(d) and 14(c).

In the standard case (Figure 15(a)), the overall curves of both $\mathrm{d}Q/\mathrm{d}d$ and $\mathrm{d}(\#/s)/\mathrm{d}d$ decline with the increase in distance due to evaporation. The droplet diameter occupying the

largest volume is approximately 50 μm. At a distance of 0.2 m, the curve of $\mathrm{d}(\#/s)/\mathrm{d}d$ exhibits a continuously decreasing distribution (refer to the black curve in Figure 15(a)) which indicates that a vigorous breakup occurs as the flow passes through the venturi. After passing through the venturi, the curve of $\mathrm{d}(\#/s)/\mathrm{d}d$ exhibits a right-skewed distribution with a peak, which verifies that the droplet breakup rate is comparable to the fast evaporation of small droplets.

In the straight liner case (Figure 15(b)), there are many droplets that are larger than 250 μm, and the values of $\mathrm{d}Q/\mathrm{d}d$ corresponding to these droplets are significant at all distances. Therefore, the overall value of $\mathrm{d}(\#/s)/\mathrm{d}d$ is relatively small. In addition, beyond a distance of 0.6 m, the values of $\mathrm{d}Q/\mathrm{d}d$ corresponding to the droplets that are larger than 250 μm do not change significantly (indicated by the circled area in Figure 15(b)), whereas the values of $\mathrm{d}Q/\mathrm{d}d$ corresponding to the droplets that are smaller than 250 μm decrease. This implies that no breakup occurs beyond a distance of 0.6 m in the straight liner case, and the decrease in the values of $\mathrm{d}Q/\mathrm{d}d$ corresponding to the droplets that are smaller than 250 μm is only due to evaporation and not due to droplet breakup. In contrast, owing to their relatively small surface-to-volume ratio, the droplets that are larger than 250 μm do not evaporate quickly, and evaporation cannot be completed before the flow reaches the outlet of the attemperator. This explains why the nonevaporated water mass flow rate ($\dot{m}_w$) in the straight liner case (without venturi) decreases at approximately the same rate as that in the standard case (with venturi) up to a distance of 0.5 m, but slows down beyond this distance, as shown in Figure 13(d). These results clearly demonstrate that the venturi thermal liner enhances droplet breakup in the attemperator by accelerating and decelerating the steam flow, resulting in rapid evaporation.

In the multi-nozzle case (Figure 15(c)), both $\mathrm{d}Q/\mathrm{d}d$ and $\mathrm{d}(\#/s)/\mathrm{d}d$ exhibit similar trends except that the values of these parameters at a distance of 0.2 m from the nozzle are generally lower than those in the standard case. This confirms that compared to the standard case, multi-nozzles produce smaller droplets that evaporate faster before they pass through the venturi. Furthermore, the curves of $\mathrm{d}(\#/s)/\mathrm{d}d$ at distances of 0.4 m and 0.6 m have a

decreasing distribution without a peak, whereas those of the standard case have a peak. This implies that even though smaller droplets are produced in the multi-nozzle case, strong breakup occurs as they flow through the venturi compared to the standard case. This phenomenon is possibly due to the droplet distribution pattern and the steam velocity profile at the venturi neck. As shown in Figure 16(a), in the standard case, most of the droplets pass through the central region of the venturi neck as the water jet is ejected from a single nozzle. As the steam flow is most accelerated in the peripheral region of the venturi neck, most droplets are not accelerated to the maximum velocity required for effective breakup. In contrast, in the multi-nozzle case, water jets are ejected from multiple nozzles, and the droplets are distributed over the entire cross-sectional area of the venturi neck (Figure 16(b)). Consequently, droplets passing through the peripheral region of the venturi neck are accelerated to their maximum velocity, resulting in additional breakup. These results indicate that besides the initial production of small droplets through multiple nozzles, the spatial distribution of the droplets is also important for breakup.

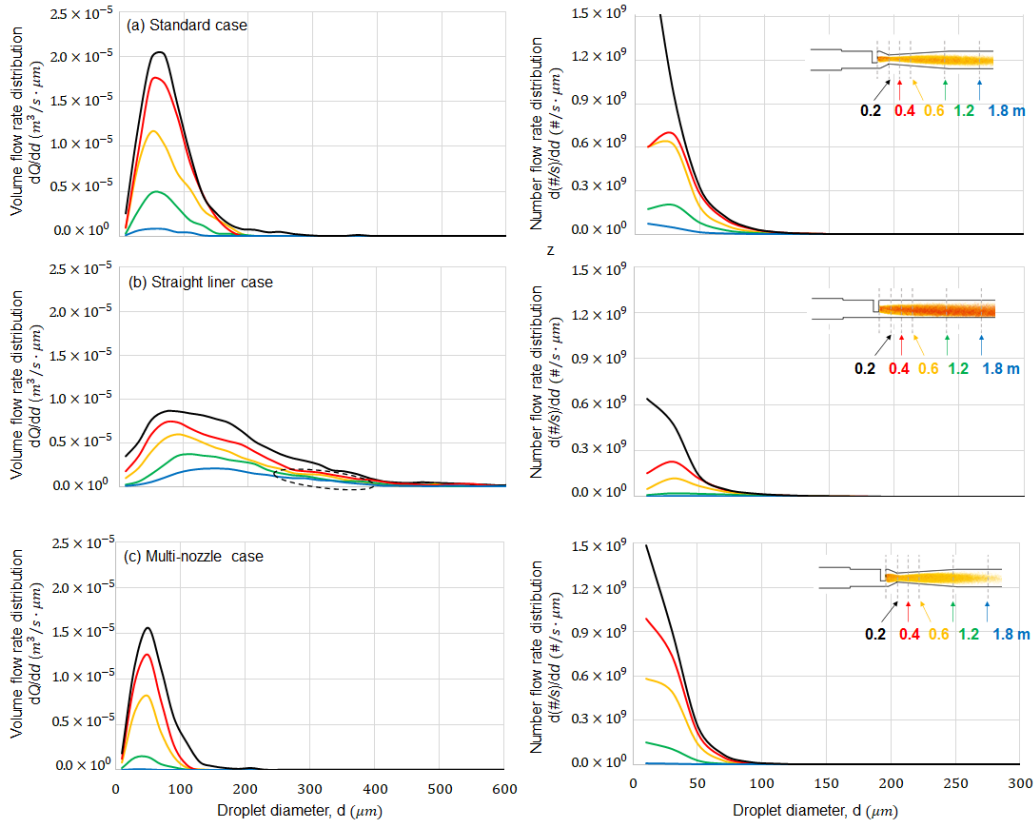

Figure 30 Distributions of the droplet volume flow rate and droplet number flow rate versus the droplet size at various distances from the nozzle: (a) standard case; (b) straight liner case; and (c) multi-nozzle case. The black, red, orange, green, and blue lines represent the distributions at 0.2 m, 0.4 m, 0.6 m, 1.2 m, and 1.8 m from the nozzle, respectively, as indicated by the inset figures in the droplet position scatter plots.

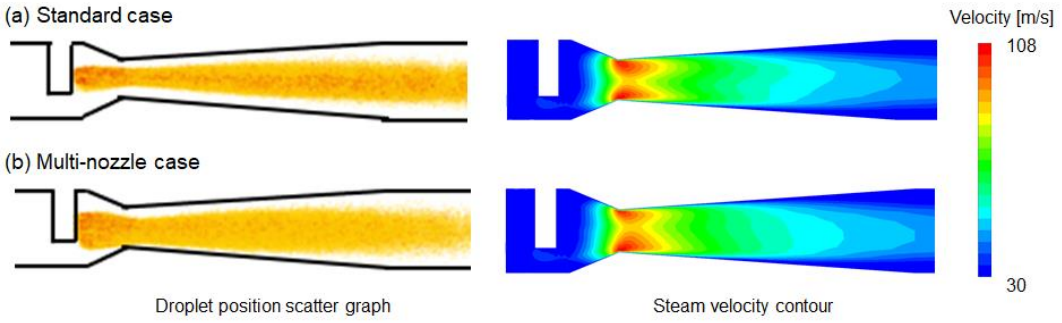

Figure 31 Droplet position scatter plots (left-hand side) and steam velocity contours (right-hand side) of: (a) standard case and (b) multi-nozzle case.

CHAPTER 7. CONCLUSIONS

By adapting the thermowell transient analysis, the steam temperatures at the inlet and the outlet of the attemperator could be better estimated from the temperatures measured by the respective thermowells. In addition, by using the fluid and pipe transient analysis, the temperature of the spray water injected into the attemperator could be reliably estimated. Using these results and the enthalpy balance, the spray water flow rate could be calculated accurately enough to discern whether the spray injected steam was completely desuperheated before reaching the outlet thermowell of the attemperator.

Comparing the outlet temperature of measured data to the results of three-dimensional simulations is not good enough to validate the simulation since the measured temperature could be not reliable. However, the transient analysis allows checking whether the sprayed water is completely evaporated or not considering the heat capacity. As a results, these results were used for the validation of three-dimensional simulations of the attemperator system.

In simulations, droplet breakup and evaporation in various attemperator design configurations were numerically simulated in the three-dimensional domain, considering both primary and secondary droplet breakup. First, the accuracy of the proposed simulation model was verified by comparing the simulation results of four commissioning conditions of the attemperator with the corresponding transient thermal analysis results from a previous study. Subsequently, four design cases—standard, symmetric, straight liner, and multi-nozzle—were simulated and compared using the validated numerical simulation model.

In the standard case, the nozzle cylinder had a single nozzle hole with a diameter of 40 mm. In addition, a venturi-type thermal liner was installed immediately after the nozzle cylinder. Initially, the primary breakup of the liquid jet ejected from the single nozzle produced droplets with a relatively wide size distribution. The jet velocity was less than 10 m/s, whereas the average steam velocity was 20 m/s in the main pipe, which accelerated to over 100 m/s after passing through the venturi. The large droplets were not accelerated as

much as the small droplets. The large droplets were broken down into smaller droplets owing to the drag force generated by the difference in velocity between the steam and the droplets (secondary breakup). This significantly increased the number of small droplets, which was verified by the number of droplets present at the venturi neck. Scatter plots of the droplet temperature revealed that the temperature of most droplets increased to the saturation temperature over very short distances, and a significant number of small droplets evaporated before they could reach the venturi neck. Notably, the temperature of the small droplets increased faster than that of the large droplets, and the former evaporated faster owing to their large surface-to-volume ratio. Therefore, in the standard case, all droplets with a diameter of less than 250 μm were completely evaporated within a distance of 0.4 m from the nozzle.

In the straight liner case, droplet breakup was less strong, and several droplets with a diameter of more than 250 μm were present at all distances. In addition, beyond a distance of 0.6 m, no breakup occurred and the droplets that were larger than 250 μm did not evaporate quickly owing to their relatively small surface-to-volume ratio. Thus, complete evaporation did not occur before the flow reached the outlet of the attemperator.

These results verify that the sprayed droplets must break down to below a certain size for complete evaporation to occur. The venturi thermal liner plays an important role in enhancing droplet breakup, resulting in fast evaporation.

In the multi-nozzle case, smaller droplets were produced owing to the smaller hole size of each nozzle. The droplets experienced additional breakup while passing through the peripheral region of the venturi neck, further decreasing the evaporation distance. These results indicate that in addition to the initial size of the droplets, their spatial distribution is important as well.

Owing to the asymmetric shape of the nozzle cylinder inside the main pipe, the steam flow was tilted to one side, increasing the likelihood of collisions between the droplets and the thermal liner wall. This problem can be resolved by making the nozzle cylinder symmetrical, as demonstrated in the symmetrical case.

REFERENCES

[1] N. Kumar, Improving the flexibility of coal-fired power plants, Power Eng. 118 (2014).

[2] A. (Energiewende), Flexibility in thermal power plants, n.d.

[3] Eng. Lab, GIZ-Thermal power plant flexibility improvements in Chile, n.d.

[4] C. Henderson, Coal-Fired Power Plants – Flexibility Options and Challenges, (2016) 32. https://www.unece.org/fileadmin/DAM/energy/se/pp/clep/ge12_ws_oct2016/04_Henderson_UNECE.Flexibility.pdf.

[5] K. Dietl, K. Link, Start up optimization of Combined Cycle Power Plants: Controller development and real plant test results, 2018 5th Int. Conf. Control. Decis. Inf. Technol. CoDIT 2018. (2018) 599–604. https://doi.org/10.1109/CoDIT.2018.8394850.

[6] MTIE, 9th Basic plan on Electricity Demand and Supply, (2020).

[7] Y. Uruno, G. Choi, M. Sung, J. Chung, H. Kim, K. Lee, Transient analysis of attemperator enthalpy balance based on the commissioning data of a coal-fired steam power plant, Appl. Therm. Eng. 150 (2019). https://doi.org/10.1016/j.applthermaleng.2019.01.047.

[8] A. Sadiki, M. Chrigui, J. Janicka, M.R. Maneshkarimi, Modeling and simulation of effects of turbulence on vaporization, mixing and combustion of liquid-fuel sprays, Flow, Turbul. Combust. 75 (2005) 105–130. https://doi.org/10.1007/s10494-005-8579-0.

[9] H. Guo, J. Wang, J. Wu, X. Du, Study on spray evaporation treatment of desulfurization wastewater, Coatings. 11 (2021) 1–19. https://doi.org/10.3390/coatings11040418.

[10] H. Montazeri, B. Blocken, J.L.M. Hensen, Evaporative cooling by water spray systems: CFD simulation, experimental validation and sensitivity analysis, Build. Environ. 83 (2015) 129–141. https://doi.org/10.1016/j.buildenv.2014.03.022.

[11] O. Samimi Abianeh, C.P. Chen, S. Mahalingam, Numerical modeling of multi-component fuel spray evaporation process, Int. J. Heat Mass Transf. 69 (2014) 44–53. https://doi.org/10.1016/j.ijheatmasstransfer.2013.10.007.

[12] K.G. Schoonover, W.M. Ren, S.M. Ghiaasiaan, S.I. Abdel-Khalik, Mechanistic modeling of desuperheater performance, ISA Trans. 35 (1996) 45–51. https://doi.org/10.1016/0019-0578(96)00006-7.

[13] E. Rahimi, S. Torfeh, R. Kouhikamali, Numerical study of counter-current desuperheaters in thermal desalination units, Desalination. 397 (2016) 140–150. https://doi.org/10.1016/j.desal.2016.06.028.

[14] R. Kouhikamali, H. Hesami, A. Ghavamian, Convective heat transfer in a mixture of cooling water and superheated steam, Int. J. Therm. Sci. 60 (2012) 205–211. https://doi.org/10.1016/j.ijthermalsci.2012.05.012.

[15] R.D. Reitz, Modeling Atomization Processes in High-Pressure Vaporizing Sprays, At. Sprays. 3 (1987) 309–337.

[16] B. Cho, G. Choi, Y. Uruno, H. Kim, J. Chung, H. Kim, K. Lee, One-dimensional simulation for attemperator based on commissioning data of coal-fired steam power plant, Appl. Therm. Eng. 113 (2017). https://doi.org/10.1016/j.applthermaleng.2016.11.069.

[17] V. Ebrahimian, M. Gorji-Bandpy, Two-dimensional modeling of water spray cooling in superheated steam, Therm. Sci. 12 (2008) 79–88. https://doi.org/10.2298/TSCI0802079E.

[18] P.J.Dechamps, Modelling the Transient Behaviour of Heat Recovery Steam Generators, Proc. Inst. Mech. Eng. Part A J. Power Energy. 209 (1995).

[19] W. Zima, Simulation of dynamics of a boiler steam superheater with an attemperator, Proc. Inst. Mech. Eng. Part A J. Power Energy. 220 (n.d.).

[20] W. Zima, Sł. Grądziel, A. Cebula, Modelling of heat and flow phenomena occuring in waterwall tubes of boilers for supercritical steam parameters, Arch. Thermodyn. 31 (2010) 19–36. https://doi.org/10.2478/v10173-010-0012-y.

[21] E.M. Sparrow, F.N.D.E. Farias, D. Engenharia, R. De Janeiro, Unsteady Heat Transfer Inlet in Ducts With, Inernational J. Heat Mass Transf. 11 (1968) 837–853.

[22] A.S.L. F.P.Incropera, D.P.DeWitt, T.L.Bergman, Fundamental heat and mass transfer, 2007.

[23] K.C. Mills, S.U. Yuchu, L.I. Zushu, R.F. Brooks, Equations for the calculation of the thermo-physical properties of stainless steel, ISIJ Int. 44 (2004) 1661–1668. https://doi.org/10.2355/isijinternational.44.1661.

[24] P.Harvey, Engineering properties of steel, 1982.

[25] H. Liang, B. Zhao, C. Huang, H. Song, X. Jiang, Numerical simulation study on performance optimization of desuperheater, Energy Reports. 7 (2021) 2221–2232. https://doi.org/10.1016/j.egyr.2021.04.023.

[26] S. V. Patankar, Numerical heat transfer and fluid flow, McGraw-Hill, n.d.

[27] P. FOX, McDONALD, Fluid Mechanics, eighth, WILEY, n.d.

[28] J. Huang, X. Zhao, Numerical simulations of atomization and evaporation in liquid jet flows, Int. J. Multiph. Flow. 119 (2019) 180–193. https://doi.org/10.1016/j.ijmultiphaseflow.2019.07.018.

[29] D. Stefanitsis, P. Koukouvinis, N. Nikolopoulos, M. Gavaises, Numerical Investigation of the Aerodynamic Droplet Breakup at Mach Numbers Greater Than 1, J. Energy Eng. 147 (2021) 04020077. https://doi.org/10.1061/(asce)ey.1943-7897.0000720.

[30] D. Stefanitsis, G. Strotos, N. Nikolopoulos, M. Gavaises, Numerical investigation of the aerodynamic breakup of a parallel moving droplet cluster, Int. J. Multiph. Flow. 121 (2019) 103123. https://doi.org/10.1016/j.ijmultiphaseflow.2019.103123.

[31] D. Stefanitsis, I. Malgarinos, G. Strotos, N. Nikolopoulos, E. Kakaras, M. Gavaises, Numerical investigation of the aerodynamic breakup of droplets in tandem, Int. J. Multiph. Flow. 113 (2019) 289–303. https://doi.org/10.1016/j.ijmultiphaseflow.2018.10.015.

[32] A.A. SAJ Morsi, An investigation of particle trajectories in two-phase flow systems, J. Fluid Mech. (1972).

[33] C. Lian, G. Xia, C.L. Merkle, Impact of source terms on reliability of CFD algorithms, Comput. Fluids. 39 (2010) 1909–1922. https://doi.org/10.1016/j.compfluid.2010.06.021.

[34] J. Zhang, T. Li, H. Ström, T. Løvås, Grid-independent Eulerian-Lagrangian approaches for simulations of solid fuel particle combustion, Chem. Eng. J. 387 (2020) 123964. https://doi.org/10.1016/j.cej.2019.123964.

[35] A.F.T. Guide, Ansys Fluent Theory Guide, ANSYS Inc., USA. 15317 (2013) 724–746.

[36] A.H. Lefebvre, V.G. McDonell, Atomization and sprays, 2017. https://doi.org/10.1201/9781315120911.

[37] P.-K. WU, L.-K. TSENG, G. FAETH, Primary breakup in gas/liquid mixing layers for turbulent liquids, (1992). https://doi.org/10.2514/6.1992-462.

[38] A.A. O'Rourke PJ, The Tab method for numerical calculation of spray droplet breakup, SAE Pap. (1987).

[39] M.R. Turner, S.S. Sazhin, J.J. Healey, C. Crua, S.B. Martynov, A breakup model for transient Diesel fuel sprays, Fuel. 97 (2012) 288–305.

https://doi.org/10.1016/j.fuel.2012.01.076.

[40] D.W. Stanton, C.J. Rutland, Modeling Fuel Film Formation and Wall Interaction in Diesel Engines, SAE Trans. 105 (1996) 808–824. http://www.jstor.org/stable/44736319.

[41] T. Bodnár, G.P. Galdi, Š. Necasová, Particles in Flows, 2017. http://link.springer.com/10.1007/978-3-319-60282-0.

[42] P.J. O'ROURKE, COLLECTIVE DROP EFFECTS ON VAPORIZING LIQUID SPRAYS, Princeton University ProQuest Dissertations Publishing, 1981.